Carbon nitride-based catalysts for thermal carbon monoxide oxidation: Does phase matter?

By

Ahmed Gamal Abdelmoneim Mohamed

A dissertation submitted to the Faculty of Science, University of the Witwatersrand, Johannesburg, in fulfilment of the requirements for the degree of Master of Science from Faculty of Science, School of Chemistry.

June 2023

Declaration

I declare that this dissertation is my own, unaided work. It is being submitted for the Degree of Master of Science at the University of the Witwatersrand, Johannesburg. It has not been submitted before for any degree or examination at any other University.

(Signature of candidate)

Signed on the 20th day of August 2023.

Abstract

Carbon monoxide (CO) has a poisonous effect on all living organisms as it binds to the hemoglobin of blood cells, preventing oxygen uptake. Thus, the conversion of CO to less dangerous gas such as CO_2 is an essential process. This work presented the utilization of carbon nitrides (C_3N_x) in different phases (βgC_3N_4, βC_3N_5, βC_3N_6) for thermal carbon monoxide (CO) oxidation. Herein, gC_3N_4, C_3N_5, and C_3N_6 were prepared by pyrolysis of their amine precursors, which were doped with Fe by two distinct methods; mechanical mixing (Fe/C_3N_x-M) and polymerization (Fe/C_3N_x-P). The controlled preparation of Fe/gC_3N_4-P allowed the formation of hierarchical porous structures with high surface area (219 m^2/g) compared to the Fe/gC_3N_4-M (77 m^2/g). This enabled the ease of reactants diffusion, enhanced the electron transfer, and maximized the atomic utilization. Accordingly, Fe/gC_3N_4-P (T_{100}= 245 °C) presented higher catalytic activity than Fe/gC_3N_4-M (T_{100}= 291 °C).

In addition, bimetallic $FeTi/gC_3N_4$-P and trimetallic $FeTiCu/gC_3N_4$-P catalysts achieved the complete conversion of carbon monoxide (CO) at lower temperatures; 175 and 147 °C, respectively, which was attributed to the enhanced reducibility, and synergistic effect of Ti and Cu. Besides, $FeTi/gC_3N_4$-P and $FeTiCu/gC_3N_4$-P showed higher catalytic activity than Pd/C commercial catalyst (T_{100}= 198 °C). In addition, the trimetallic $FeTiCu/gC_3N_4$-P showed a stable catalytic behavior without any deactivation for more than ten hours. This study showed that the C_3N_x phases worked successfully in the thermal catalytic CO oxidation. However, the gC_3N_4 phase is the most active one when doped with metal(s), as it offered higher crystallinity, graphitization, and thermal stability than C_3N_5 and C_3N_6. This study also paves the way for the utilization of gC_3N_4 as a support for different metals to be used efficiently in various thermal catalytic applications, not only CO Oxidation.

Acknowledgements

My heartfelt gratitude goes to my supervisors, Prof. Kenneth I. Ozoemena, Prof. Aboubakr M. Abdullah, and Dr. Kamel Eid for their guidance. I appreciate the comments, advice, and lessonslearnt throughout the duration of the course. I would also like to acknowledge the staff of the Central Laboratories Unit (CLU) of Qatar University, who helped me a lot to finalize the samples' characterization and the Gas Processing Center (GPC) for allowing me to use all the available facilities. I would also like to acknowledge my friend Dr. Adewali Ipadeola, who provided me during this journey by a lot of advice and comments. Finally, I would also like to acknowledge my parents, wife, children, and siblings.

Table of Contents

Abstract ii

Acknowledgements iv

Table of Contents v

List of Figures viii

List of Tables xi

List of Abbreviations and Symbols xii

RESEARCH OUTPUTS xviii

Chapter 1 15

Introduction 15

1.1 Introduction 15

1.2 Aim and Objectives 16

1.2.1 Aim 16

1.2.2 Objectives 17

1.2.3 Scope of Research Project 18

Chapter 2 20

Literature Review 20

2.1. Literature Survey 20

2.2. CO oxidation Mechanism 21

Chapter 3 26

Materials and Methods 26

3.1 Materials 26

3.2 Experimental Setup 27

3.3 Catalyst synthesis 27

3.3.1.Synthesis of C_3N_x phases 27
3.3.2. Synthesis of Fe/C_3N_x 28
3.3.2. Synthesis of Fe/gC_3N_4 by the polymerization method 28

3.4. Characterization Techniques 31

3.4.1. Scanning Electron Microscopy (SEM) 31
3.4.2. X-Ray Diffraction (XRD) 31
3.4.3. Fourier transform infrared (FTIR) 32
3.4.4. X-ray photoelectron spectroscopy (XPS) 32
3.4.5. BET Surface Area 32
3.4.6. Temperature programmed Reduction (H_2-TPR) 32
3.4.7. CO- Temperature Programmed desorption (CO-TPD) 33
3.4.8. Raman Analysis 33
3.4.9. Thermal Gravimetric Analysis (TGA) 33

Chapter 4 34
Exploring the catalytic properties of C_3N_x phases (x = 4, 5, 6)

4.1. Results and discussion
4.1.1. Characterization
4.1.2. Catalytic Tests 40
4.2. Conclusions 40

Chapter 5 40
Catalytic performance of Fe-doped catalysts; Fe/gC_3N_4, Fe/C_3N_5, and Fe/C_3N_6
5.1. Results and discussoin
5.1.1. Characterization 41
5.1.2. Catalytic Tests……..47

5.2. Conclusions 48

Chapter 6 49

Catalytic performance of Fe/gC3N4-M prepared by mechanical mixing and Fe/gC3N4-P synthesized by the polymerization method

6.1. Results and discussion

6.1.1. Characterization 49

6.1.2 Catalytic Tests 52

6.2. Conclusions 54

Chapter 7 55

Catalytic performance of the monometallic, bimetallic, and trimetallic catalysts; Fe/gC_3N_4-P, FeTi/gC_3N_4-P, and FeTiCu/gC_3N_4-P

7.1. Results and discussion

7.1.1. Characterization 55

7.1.2 Catalytic Tests 60

7.2. Conclusions 64

Chapter 8 66

Conclusions and perspectives

8.1. Conclusions 66

8.2. perspectives 70

References 72

Appendix 81

List of Figures

Figure 1.1. A schematic diagram illustrates the designed work plan..... 19

Figure 2.1. Publications number in the last decade, data obtained from Scopus. 22

Figure 3.1. A schematic diagram shows the used experimental setup..... 27

Figure 3.2. The chemical structure depictions of (a) gC_3N_4, (b) C_3N_5, and (c) C_3N_6. 28

Figure 3.3. Real pictures for the prepared C_3N_x phases (upper side) and Fe/C_3N_x catalysts prepared by mechanical mixing.....30

Figure 3.4. The proposed fabrication mechanism of Fe/gC_3N_4-P..... 31

Figure 4.1. (a) FTIR and (b) XRD of the three C_3N_x phases……..…….35

Figure 4.2. SEM images and EDX analysis of the three C_3N_x phases…….36

Figure 4.3. XPS analysis of the three C_3N_x phases

(a) XPS-Full surface Survey……..… 37

(b-c) High-resolution C1s XPS spectra and its interpretation…….……..…..37

(d-e) High-resolution N1s XPS spectra and its interpretation……37

Figure 4.4a: TGA of gC_3N_4, C_3N_5, and C_3N_6……..…..……..….39

Figure 4.4b: Raman analysis of gC_3N_4, C_3N_5, and C_3N_6……...……...39

Figure 5.1.

(a) FTIR of the Fe/C_3N_x catalysts ……..…….…….……42

(b) FTIR of the C_3N_x phases…..…….42

(c) XRD of the Fe/C_3N_x catalysts…….…….42

(d) XRD of the C_3N_x phases…….…….42

Figure 5.2. SEM and EDX of

(a) Fe/gC_3N_4...…….43

(b) Fe/C_3N_5...…….43

(c) Fe/C_3N_6...……...…….43

(d) EDX ...…….…….…….43

Figure 5.3. XPS analysis of Fe/gC_3N_4, Fe/C_3N_5, and Fe/C_3N_6

(a) XPS-Full surface Survey ……..…...……44

(b-c) High-resolution C1s XPS spectra and its interpretation……...……44

(d-e) High-resolution N1s XPS spectra and its interpretation……..…..44

(f-g) High-resolution XPS spectra of Fe2p…….44

Figure 5.4. TGA and Raman analyses

(a) TGA of C_3N_x phases and their catalysts…….…….…….……..46

(b) TGA of Fe/gC_3N_4, Fe/C_3N_5, and Fe/C_3N_6…….…….46

(c) Raman analyses of C_3N_x phases and their catalysts.....….46

(d) Raman analyses of Fe/gC_3N_4, Fe/C_3N_5, and Fe/C_3N_6……..…….…….…….46

Figure 5.5. (a) Catalytic activity and (b) reaction kinetics of Fe/gC_3N_4, Fe/C_3N_5, and Fe/C_3N_6.....47

Figure 6.1.

(a) FTIR, (b) XRD, and (c) (EDX) of Fe/gC_3N_4-M and Fe/gC_3N_4-P…….....……..50

(d) SEM image of Fe/gC_3N_4-M, and (e-h) SEM images of Fe/gC_3N_4-P ……...….50

Figure 6.2. N_2 adsorption-desorption isotherms of (a) Fe/gC_3N_4-P, (b) Fe/gC_3N_4-M, and (c) pore size distribution of Fe/gC_3N_4-P……..…...……52

(d) XPS full surface survey of Fe/gC_3N_4-M and Fe/gC_3N_4-P, (e) C1s spectra, (f) N1s spectra, and (g) Fe2p spectra of Fe/gC_3N_4-P……..……...52

Figure 6.3. (a)TGA, (b) Raman, (c) catalytic tests, and (d) kinetic reactions of Fe/gC_3N_4-M and Fe/gC_3N_4-P……..……..53

Figure 7.1. FTIR (a), XRD (b), and EDX (c) of Fe/gC_3N_4-P, FeTi/gC_3N_4-P, and FeTiCu/gC_3N_4-P SEM images of (d) Fe/gC3N4-P, (e) FeTi/gC_3N_4-P, and (f) FeTiCu/gC_3N_4-P……56

Figure 7.2. XPS Analysis

(a) full surface survey…….…….……58

(b-c) High-resolution spectra of C1s and its interpretation……...…….…….……58

(d-e) High-resolution spectra of N1s and its interpretation…….58

(f-g) High-resolution spectra of Fe2p and its interpretation……...……..…58

(h-i) High-resolution spectra of Ti2p and its interpretation……...……..58

(j) High-resolution spectra of Cu2p and its interpretation……..…….58

Figure 7.3. TGA (a), Raman (b), H_2-TPR (c), and CO-TPD of Fe/gC_3N_4-P, FeTi/gC_3N_4-P, and FeTiCu/gC_3N_4-P……60

Figure 7.4. Catalytic activity (a) and kinetic reactions (b) of Fe/gC_3N_4, FeTi/gC_3N_4, FeTiCu/gC_3N_4 ……..…..……...……..63

(c) Reproducibility tests and (d) stability test of FeTiCu/gC_3N_4……...……...…...……..63

Figure 7.5. A comparison

(a) between FeTiCu/gC_3N_4 and Pd/C-Comm…….64

(b) among the gC_3N_4 based catalysts and Pd/C-Comm……...…….64

List of Tables

Tale 2.1: Examples of C_3N_x phases, their preparation methods, and applications……..22

Tale 2.2: List of all reported C_3N_x -based catalysts for thermal CO oxidation……...24

Table 3.1: A summary of the preparation conditions of all synthesized samples……31

Table 4.1: CHNSO analysis of the C_3N_x phases…….....39

Table 5.1: CHNSO analysis of the Fe/C_3N_x catalysts….....46

Table 6.1: BET surface area measurements of all samples……..53

Table 7.1: A comparison among the as-synthesized gC_3N_4 based catalysts….....62

Table 8.1: A comparison among different catalysts ……...…….67

List of Abbreviations and Symbols

- C_3N_x: Carbon nitride phases
- gC_3N_4: graphitic carbon nitride phase
- Fe: Iron
- Ti: Titanium
- Cu: Copper
- Au: Gold
- Co: Cobalt
- Pd: Palladium
- Pt: Platinum
- C_2H_5OH: Ethanol
- $Fe(NO_3)_3 \cdot 9H_2O$: Iron(III) nitrate nonahydrate
- $C_{12}H_{28}O_4Ti$: Titanium (IV) isopropoxide
- $C_3H_6N_6$: Melamine
- HNO_3: Nitric acid
- $Cu(NO_3)_2 \cdot 3H_2O$: Copper(II) nitrate trihydrate
- CNFs: Carbon nanofibers
- CNTs: Carbon nanotubes
- MFC: Mass Flaw controller
- MS: Mass Spectrometer
- GC: Gas chromatograph
- g: gram
- L: Liter
- h: Hour
- ml: Milliliter

- min.: Minute
- °C: Degree Celsius
- (g): gas
- ads.: adsorbed
- CO: Carbon monoxide
- T_{100}: Temperature of Complete CO Conversion
- CO_2: Carbon dioxide
- O_2: Oxygen
- Ar: Argon
- N_2: Nitrogen
- H_2: Hydrogen
- H_2O: Water
- mg: Milligram
- mmol: millimole
- vol.%: Volume percentage
- wt.%: weight percentage
- IR: Infrared
- FTIR: Fourier-transform infrared spectroscopy
- BET: Brunauer-Emmett-Teller
- BJH: Barret-Joyner-Halender method
- H_2-TPR: Hydrogen Temperature Programmed Reduction
- TPO: Temperature Programmed Oxidation
- CO-TPD: Carbon Monoxide Temperature Programmed Desorption
- TCD: Thermal Conductivity Detector
- SEM: Scanning electron microscopy
- TEM: Transmission electron microscopy

- XRD: X-ray diffraction
- XPS: X-ray photoelectron spectroscopy
- Fe/C_3N_x-M: Catalysts prepared by mechanical mixing
- Fe/C_3N_x -P: Catalysts prepared by polymerization of melamine
- Pd/C-Comm.: Commercial palladium catalyst
- BET: Brunauer, Emmett and Teller
- BJH: Barrett-Joyner-Halenda
- BE: Binding Energy

RESEARCH OUTPUTS

Manuscripts have been prepared for publications

Journal Manuscripts:

1. **Ahmed Gamal,** Kamel Eid, Aboubakr M. Abdullah, and Kenneth I Ozoemena *"Effect of carbon nitride phase on the catalytic activity of Fe-doped carbon nitride nanocomposite towards CO thermal oxidation"* ***(submitted)***
2. **Ahmed Gamal,** Kamel Eid, Aboubakr M. Abdullah, and Kenneth I Ozoemena *"Rational Synthesis of gC_3N_4-Based catalysts doped with Fe and Ti, for Catalytic CO Oxidation"* ***(Ready to be submitted)***
3. **Ahmed Gamal,** Kamel Eid, Aboubakr M. Abdullah, and Kenneth I Ozoemena "*Mono, Bi, and Tri-metallic gC_3N_4-Based Catalysts for Thermal catalytic CO oxidation"* ***(Ready to be submitted)***
4. **Ahmed Gamal**, Mostafa H. Sliem, Kamel Eid, Aboubakr M. Abdullah, and Kenneth I Ozoemena "*Open-Mouthed Nanocapsules Ru-Based catalyst for Catalytic CO Oxidation"* ***(Ready to be submitted)***
5. **Ahmed Gamal**, Adewale K. Ipadeola, Kamel Eid, Aboubakr M. Abdullah, and Kenneth I Ozoemena *" Pt-based Catalysts for Methane Steam Reforming; A review"* ***(Ready to be submitted)***

Conference abstracts and presentations:

1. **Ahmed Gamal**, Kamel Eid, Aboubakr M. Abdullah, and Kenneth I Ozoemena " *Rational*

Synthesis of gC_3N_4 Nanostructures doped with Fe for Thermal Catalytic CO Oxidation" ***(Submitted to ACS Fall 2023)***

2. **Ahmed Gamal**, Mostafa H. Sliem, Kamel Eid, Aboubakr M. Abdullah, and Kenneth I Ozoemena "*Open-Mouthed Nanocapsules $Ru@gC_3N_4$ for Thermal Catalytic CO Oxidation.* ***(Submitted to the 18th Qatar Gas Engineering Forum)***

Chapter 1
Introduction

1.1. Introduction

Reducing carbon monoxide (CO) in the atmosphere is a vital process, as CO is a poisonous gas that can cause the immediate death by combining with the hemoglobin of the blood cell faster than oxygen [1-3]. Conversion of CO to CO_2 is a highly attractive way to decrease the CO emissions as it possesses many advantages such as simplicity, and low activation energy [4, 5]. In addition, CO oxidation to CO_2 (equation 1)[6, 7] is important in fundamental and industrial applications[8, 9]. Various noble metals, such as gold (Au), palladium (Pd), and platinum (Pt) [10, 11], and transition metals, such as iron (Fe), copper (Cu), and cobalt (Co) [12-14] were reported for the CO oxidation process. However, noble metals' high cost and scarcity preclude their larger use.

$$2CO + O_2 \rightarrow 2CO_2 \quad \Delta H = -566\ kJ/mol. \qquad Eqn.\ 1$$

Different materials were reported as supports for the noble and transition metals such as silica and alumina. However, π-conjugated polymer carbon nitride (C_3N_x) has attracted many researchers to investigate it in various catalytic reactions in the last ten years, owing to its catalytic, photocatalytic, electronic structure, and physiochemical merits in addition to its cheap price [15-17]. However, carbon nitride (C_3N_x, x = 4, 5, 6), with different phases, is rarely reported for the thermal catalytic reactions, particularly thermal CO oxidation, as only 14 articles were reported using graphitic carbon nitride (gC_3N_4) phase as a support. On the other hand, the two phases; C_3N_5 and C_3N_6 have not been studied for the thermal oxidation of carbon monoxide. Moreover, none of those 14 articles investigated the iron (Fe) on the graphitic carbon nitride (gC_3N_4) as a catalyst for thermal CO oxidation.

Herein, this study is devoted to exploring the carbon nitride phases, i.e., gC_3N_4, C_3N_5, and C_3N_6, which were synthesized by the pyrolysis of melamine[18], aminotriazole[19], and aminoguanidine hydrochloride[20], respectively. In addition, investigating their supporting role in the thermal catalytic oxidation of carbon monoxide, especially, the phases; C_3N_5 and C_3N_6 that have not been investigated as supports with any metal in the thermal oxidation of carbon monoxide. Moreover, this work investigates the impact of Fe and Ti on the gC_3N_4, which has not been reported for the thermal CO oxidation. However, Fe and Ti were reported intensively with other supports for the CO oxidation and showed enhanced effect for the CO oxidation [21, 22]. Moreover, this study provides a comparison between the catalytic performance of Fe-doped gC_3N_4 prepared by the traditional mechanical mixing (T_{100}291) and the one prepared by the polymerization method (T_{100}245) to achieve better catalytic activity as the recent polymerization method is reported to offer porous structures with high surface area, which subsequently enhance the catalytic performance. Furthermore, the monometallic, bimetallic, and trimetallic effect on the catalytic performance has been investigated by preparing Fe/gC_3N_4-P, FeTi/gC_3N_4-P, and FeTiCu/gC_3N_4-P, which achieved the complete CO conversion at 245, 175, and 147 °C, respectively.

1.2. Aim and Objectives

1.2.1 Aim

The aim of this study is to investigate the different carbon nitride phases and their role in the oxidation of carbon monoxide, especially the phases; C_3N_5 and C_3N_6 phases that have not been reported for the oxidation of carbon monoxide.

1.2.2 Objectives

The aim was achieved through the following objectives, schematically illustrated with precise

work plan as shown in Figure 1.1

- Synthesis of the different phases of graphitic carbon nitride (gC_3N_4, C_3N_5, and C_3N_6) and exploring the differences.
- Characterization of all prepared samples through different techniques, such as XPS, SEM, XRD, FTIR, TGA, and Raman.
- Preparation and evaluation of the carbon nitride based catalysts (Fe/gC_3N_4, Fe/C_3N_5, and Fe/C_3N_6) in the catalytic thermal CO oxidation.
- Exploring the impact of Ti and Cu as bimetallic $FeTi/gC_3N_4$ and trimetallic $FeTiCu/gC_3N_4$ catalysts on the catalytic performance.
- Examining all catalysts for the thermal CO oxidation and figuring out the best catalyst that show the highest catalytic performance and can compete the commercial catalysts.

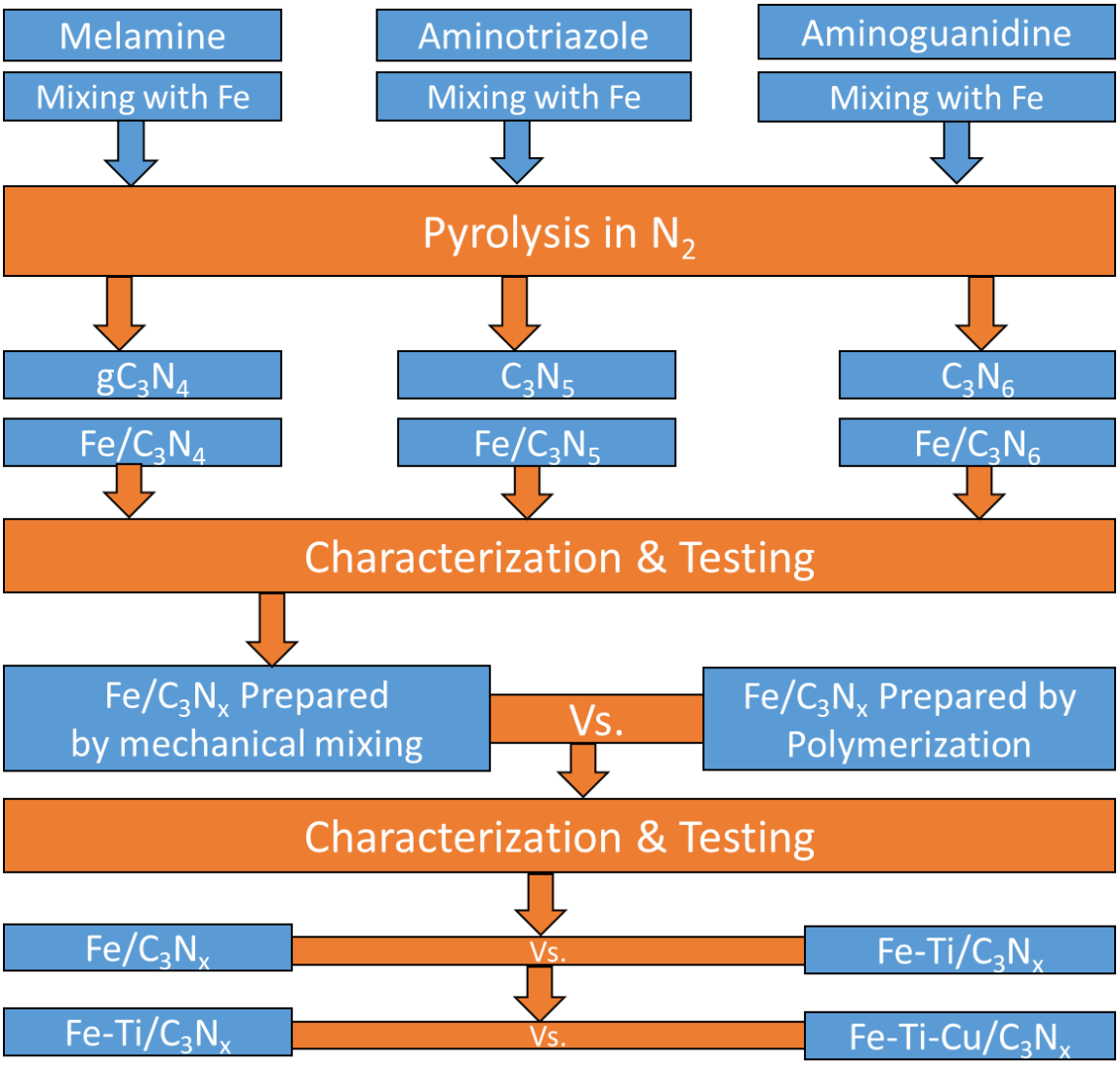

Figure 1.1. A schematic diagram illustrates the designed work plan

1.3. Scope of Research Project

Chapter 1: Introduction

This chapter shows the poisonous effect of CO on the living organisms and the common materials used in the CO oxidation process to reduce the CO in the atmosphere. In addition, this chapter includes the reasons of choosing the carbon nitride materials to be tested in the CO oxidation and the advantages of using Fe, Ti, and Cu with the carbon nitride.

Chapter 2: Literature Review

This chapter focuses on an introduction of the publications on carbon nitride based materials, the used applications and the developments of catalysts.

Chapter 3: Methodology

This chapter discuss the used synthesis methods (mechanical mixing and polymerization by HNO_3) and explain the differences of each process and the materials used to prepare the catalysts. In addition, this chapter presents the experimental techniques and the machines used to characterize the samples.

Chapter 4: Exploring the catalytic properties of C_3N_x phases ($x = 4, 5, 6$)

This chapter discusses the differences of the carbon nitride phases (gC_3N_4, C_3N_5, and C_3N_6) and comparing their catalytic properties.

Chapter 5: Catalytic performance of Fe-doped catalysts; Fe/gC_3N_4, Fe/C_3N_5, and Fe/C_3N_6

This chapter focuses on the differences of the Fe/gC_3N_4-M, Fe/C_3N_5-M, and Fe/C_3N_6-M and comparing their catalytic performance in the CO oxidation.

Chapter 6: Catalytic performance of Fe/gC_3N_4-M prepared by mechanical mixing and Fe/gC_3N_4-P synthesized by the polymerization method

This chapter investigates the catalytic performance of Fe/gC_3N_4-M prepared by mechanical mixing and Fe/gC_3N_4-P prepared by the polymerization method.

Chapter 7: Catalytic performance of the monometallic, bimetallic, and trimetallic catalysts; Fe/gC_3N_4-P, $FeTi/gC_3N_4$-P, and $FeTiCu/gC_3N_4$-P

This chapter evaluates the catalytic performance of the monometallic, bimetallic, and trimetallic catalysts; Fe/gC_3N_4-P, $FeTi/gC_3N_4$-P, and $FeTiCu/gC_3N_4$-P in the CO oxidation. In addition, it provides a comprehensive comparison among the properties of them using different characterization techniques, such as XRD, FTIR, Raman, and H_2-TPR.

Chapter 8: Conclusions and perspectives

This chapter shows the concluded differences among the three carbon nitride phases. In addition, it summarizes the results of the catalytic performance of all tested catalysts and presents recommendations for optimizing the CO oxidation process.

Chapter 2
Literature Review

2.1. Literature Survey

In addition to the poisonous effect of CO on organisms, CO further affects the environment, as it is considered a greenhouse gas raising global warming[23]. CO can react with the (OH) radicals, decreasing its concentration in the atmosphere, while those (OH) radicals decrease the lifetime of the greenhouse gases, such as methane and carbon dioxide. It is reported that the transportation sector occupies around 90% of the anthropogenic CO emissions[24] due to the exponential growth of the population and the high demand for more transportation, as mobile vehicles have become a vital need for everyone nowadays[24]. The reason of CO emissions from engines is the incomplete combustion of the fuel and the partial oxidation of carbon occurs inside the engine producing CO, which increases with decreasing the efficiency of the engine[24]. Thus, all vehicle manufacturers were forced to attach a catalytic converter containing catalysts to the vehicles' exhaust to convert the produced CO to CO_2. Various noble metals such as Pt, Pd, and Au[10, 11] and transition metals such as Fe, Cu, and Co[12-14] were developed for the CO oxidation. However, noble metals' high cost and earth rarity are decisive barriers for large use. Unlike those noble metal-based catalysts, the transition metal-based catalysts are cheap and available. Therefore, they can replace the noble metal-based catalysts in the CO oxidation process but with some modifications and optimizations that can be carried out through the synthesis of the catalysts.

In the last ten years, there is an observed interest in investigating the C_3N_x phases in different catalytic reactions, which is indicated by the number of publications on carbon nitride, which reached around 8238 articles, according to the Web of Science. However, only 27 articles were published on the carbon nitride used in the thermal oxidation of carbon monoxide (Figure 2.1). Moreover, only 14 papers out of the 27 studied the thermal oxidation of carbon monoxide and the rest of papers were reported on the photochemical, electrochemical, and theoretical studies. Furthermore, the gC_3N_4 is the only investigated phase in the thermal oxidation of carbon monoxide and the other C_3N_5 and C_3N_6, have not been reported in any other thermal reaction.

C_3N_x have been reported to be synthesized by the pyrolysis of carbon nitride sources such as urea or melamine[18], aminotriazole[19], and aminoguanidine hydrochloride[20], to produce gC_3N_4, C_3N_5 and C_3N_6, respectively. Table 2.1 illustrates some of examples of C_3N_x phases that were reported in addition to their synthesis techniques and the application in which they are used. Table 2.2 shows the reported gC_3N_4-based catalysts that worked successfully in the thermal oxidation of carbon monoxide. Some transition metals, such as Co and Cu, Fe has not been reported on the gC_3N_4 for thermal CO oxidation and there is no any trimetallic catalysts on the gC_3N_4 reported for the thermal CO oxidation. Thus, we have chosen the Fe to be the doped metal into the C_3N_x in addition to prepare bimetallic and trimetallic catalysts by addition of Ti and Cu, respectively, and exploring their catalytic performance in thermal CO oxidation.

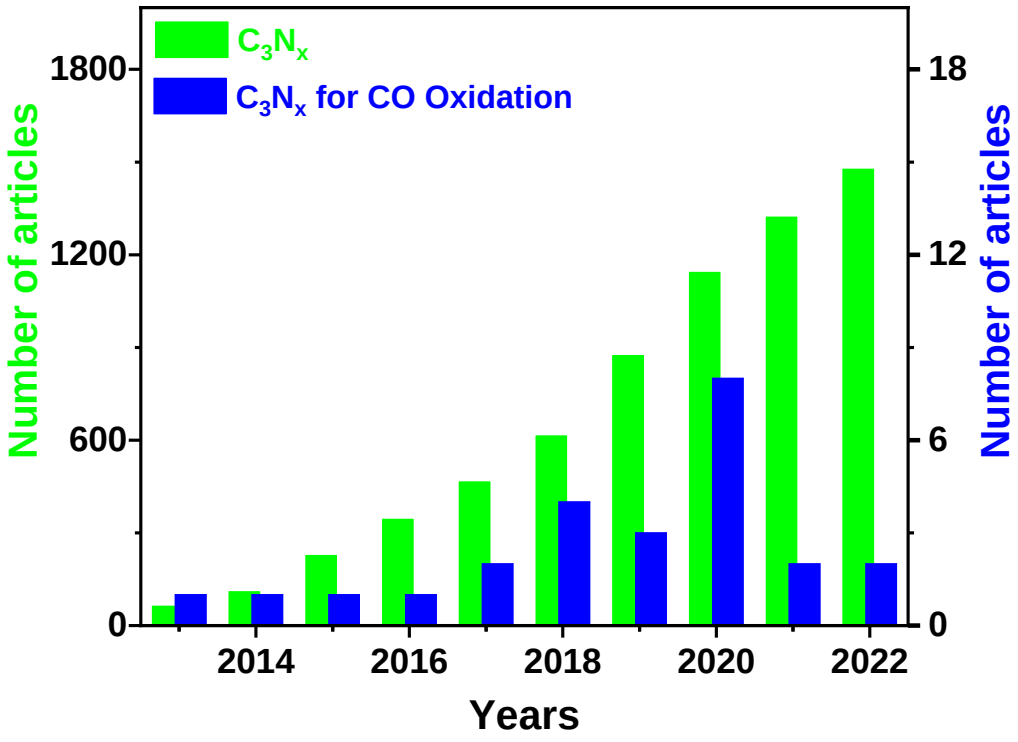

Figure 2.1. Publications number in the last ten years, collected data from Web of Science.

Table 2.1 Samples of reported C_3N_x-based catalysts

Sample	**C_3N_x Precursor**	**C_3N_x Preparation**	**Reaction**	**Ref.**
Au-Pd/g-C_3N_4	Melamine	Polymerization of melamine and then calcination at 550 °C	CO oxidation	[5]
Pt/C_3N_5	Amino-triazole	Pyrolysis at 500 °C	Hydrogen production	[25]
CNs@C_3N_5	Amino-tetrazole	Pyrolysis at 400 °C	Oxygen reduction	[26]
P-C_3N_5	Amino-triazole	Pyrolysis at 500 °C	Photoelectrochemical water splitting (PEC)	[19]
C_3N_6	Aminoguanidine	Pyrolysis at 400 °C	Photocatalytic H_2	[20]

	hydrochloride		production	
Z-C_3N_6	Aminoguanidine hydrochloride	Pyrolysis at 400 °C	Adsorption of carbondioxide	[27]

Tale 2.2 Reported C_3N_x -based catalysts for oxidation of carbon monoxide

Sample	**gC_3N_4 Preparation Method**	**Activation**	**T_{100} (°C)**	**Ref.**
Au-C_3N_4/SiO_2	Pyrolysis	Hydrogen at 300 °C	350	[28]
Pt-SBA15	Pyrolysis	/	250	[29]
Pt-CN_x/SBA15			160	[29]
Cu_2O-C_3N_4(2)	Pyrolysis	/	220	[30]
Cu_2O-gC_3N_4(3)			210	[30]
Cu_2O-gC_3N_4(4)			200	[30]
Co_3O_4-C_3N_4	Pyrolysis	/	120	[31]
Co_3O_4-gCN	Hydrothermal Treatment	/	200	[32]
Co_3O_4-$_{mpg}CN_{(0.75)}$			160	[32]
Co_3O_4-$_{mpg}CN_{(1.0)}$			160	[32]
Co_3O_4-$_{mpg}CN_{(1.25)}$			160	[32]
Co-CN/MCF	Hydrothermal Treatment	/	225	[33]
Co-CN/SBA(15)			200	[33]
Co-CN/SBA(16)			175	[33]
Pt/CN-600	Pyrolysis	/	130	[22]

Pt/CN-650 Pt/CN-700			100 85	[22] [22]
Pd/CN NWs PdCu/CNNWs	Melamine Polymerization, then pyrolysis	Hydrogen at 250 °C	250 149	[34] [34]
Au/Pd/gC_3N_4NTs	Polymerization of melamine, then pyrolysis	Hydrogen at 250 °C	165	[35]
Pd/gC_3N_4NTs Cu/gC_3N_4NTs Pd/Cu/gC_3N_4-NTs	Polymerization of melamine, then pyrolysis	Hydrogen at 250 °C	210 250 154	[2] [2] [2]
Pd/gC_3N_4NFs Au/gC_3N_4NFs Au/Pd/gC_3N_4NFs	Polymerization of melamine, then pyrolysis	O_2 then 5%H_2/He at 250 °C	191 205 144	[5] [5] [5]

2.2. Thermal CO Oxidation Mechanism

The most two common CO oxidation mechanisms are Mars-van Krevelen (MvK) and Langmuir-Hinshelwood (LH) mechanisms. MvK mechanism suggests that CO and O_2 molecules are adsorbed first into the catalyst's surface. Then the adsorbed O_2 molecule splits into individual oxygen atoms, which tend to be dispersed on the metal surface to combine with the CO molecule to form the CO_2 [36-38]. Finally, the CO_2 desorbs into the gas phase and accordingly, the reaction rate is controlled by the O_2 dissociation and CO adsorption, which usually occur at high temperatures (Equations 2-4) [36-38]. On the other hand, LH mechanism suggests that both CO and O_2 are adsorbed. Then the adsorbed CO combines with the adsorbed oxygen either in the molecular form or in the

dissociated phase to form CO_2, which finally desorbs into the gas phase [36, 38, 39]. In addition, other researchers reported another mechanism called Eley-Rideal (ER) mechanism, in which they suggest that the gas phase CO molecule directly reacts with the adsorbed oxygen producing CO_2 (Equation 5) [40, 41].

$$O_2(g) \rightarrow 2O\ ads. \qquad Eqn.2$$

$$CO\ (g) \rightarrow CO\ ads. \qquad Eqn.3$$

$$CO\ ads + O\ ads. \rightarrow CO_2(g) \qquad Eqn.4$$

$$CO\ (g) + O\ ads. \rightarrow CO_2(g) \qquad Eqn.5$$

Chapter 3
Materials and Methods

3.1 Materials

- **C_3N_x Precursors:**

  For gC_3N_4 Preparation: Melamine was used, which is also named 2,4,6-Triamino-1,3,5-triazine. ($C_3H_6N_6$ 99%)

  For C_3N_5 Preparation: Aminotriazole was used, which is also called Amitrole or 3-amino-1,2,4-triazole. ($C_2H_4N_4 \geq 95\%$)

  For C_3N_6 Preparation: Aminoguanidine hydrochloride, which is also named Guanylhydrazine hydrochloride. ($CH_7ClN_4 \geq 98\%$)

  All C_3N_x Precursors were purchased from Sigma-Aldrich.

  - **Metals Precursors:** Iron (III) nitrate nonahydrate ($Fe(NO_3)_3.9H_2O$, ≥ 99%), Titanium (IV) isopropoxide ($C_{12}H_{28}O_4Ti$ ≥ 97%), and Copper (II) nitrate trihydrate ($Cu(NO_3)_2 .3H_2O$ 99%) were provided by Scientific Global Lab Supplies W.L.L..

- **Gases:** Nitrogen gas cylinder (Pure, 50L, 150 bar, Grade 5), Oxygen gas cylinder (10vol.% O_2/Ar, 40L, 150 bar, Grade 5), Hydrogen gas cylinder (10vol.% H_2/Ar, 40L, 150 bar, Grade 5), and mixed gas cylinder 4vol.% CO, 20vol.% O_2, and balanced in Ar (40L, 150 bar, Grade 5) were supplied by Buzwair Industrial Gases Factories.
- **Solvents:** Ethanol (C_2H_6O, 99 %) and nitric acid (HNO_3 70 %) were supplied by Scientific Global Lab Supplies W.L.L.

3.2. Experimental Setup

The catalytic tests were performed using a fixed bed reactor under the atmospheric pressure (Figure 3.1). 0.05 g of the sample was put in a quartz tube (with length 40 cm and 0.6 cm diameter) between two pieces of quart wool. The outlet gas line was attached to MS, mass spectrometer (Hiden-HPR20) to measure the non-converted carbon monoxide (Figure A2). The catalysts were activated by oxidation using 20 mL/min of 10 vol.% O_2/Ar for 1 hour at 400 °C, followed by reduction using 20 mL/min of 10 vol.% H_2/Ar for another 1 hour at 400 °C as well. Then, the system was cooled to 25 °C, and the feed gas of the reaction was introduced to the catalysts, which was 20 mL/min of 4 vol.% CO and 20 vol.% of O_2 in argon. The flow rates were controlled using specific mass flow controllers (MFC) from Bronkhorst, Netherland. The temperature was raised up from 25 °C to 400 °C with a heating rate of 5 °C/min. Finally, the conversion of carbon monoxide (%CO) was calculated via equation 6.

$$\%CO = [(nCO_{in} - nCO_{out}) / nCO_{in}] * 100 \qquad Eqn.\ 6$$

Where CO_{in} is the amount of the feed-in gas and CO_{Out} is the output amount.

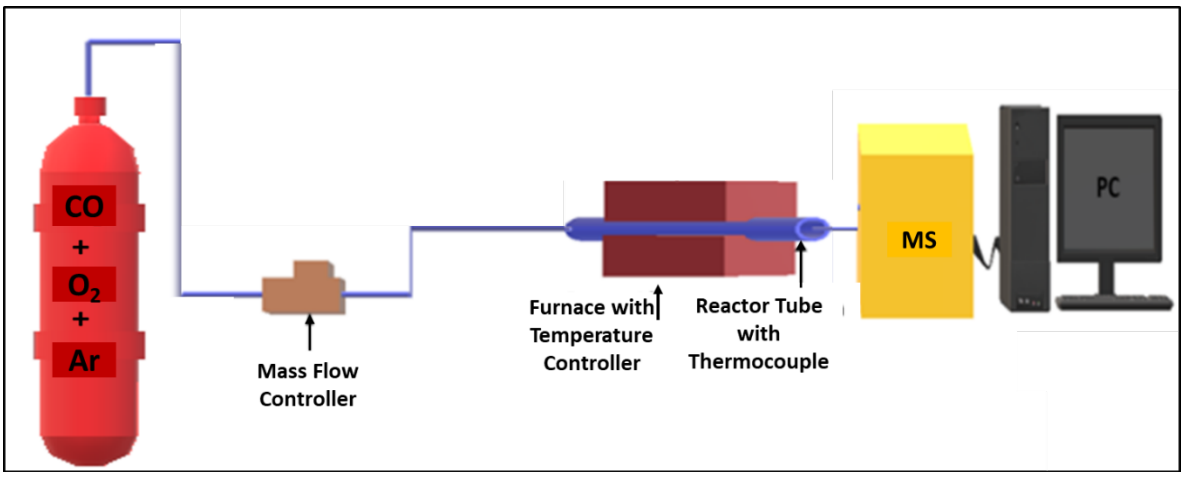

Figure 3.1. A schematic diagram shows the used experimental setup.

3.3. Catalyst synthesis

3.3.1. Synthesis of C_3N_x phases

The three carbon nitride phases (gC_3N_4, C_3N_5, and C_3N_6) were prepared by the traditional pyrolysis at high operating temperatures in N_2 atmosphere for three hours in a tubular furnace using heating rate 5 °C/min. 5g of each precursor was used to obtain the desired phase (Figure 3.2) as follows:

First: gC_3N_4 was prepared from melamine, which decomposes thermally to gC_3N_4 at 550 °C under N_2 [42, 43].

Second: C_3N_5 was prepared from aminotriazole, which decomposes thermally to C_3N_5 at 500 °C under N_2 [19, 25].

Third: C_3N_6 was prepared from aminoguanidine hydrochloride, which thermally decomposes to C_3N_6 at 400 °C under N_2 [20, 44].

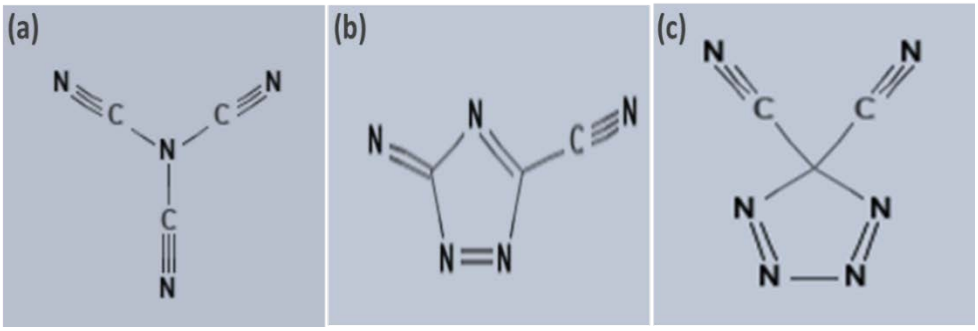

Figure 3.2. The proposed chemical structure of (a) gC_3N_4, (b) C_3N_5, and (c) C_3N_6 after pyrolysis of melamine, aminotriazole, and aminoguanidine hydrochloride, respectively.

3.3.2. Synthesis of Fe/C_3N_x catalysts

Fe/C_3N_x Catalysts were prepared by the mechanical mixing of iron (III) nitrate nonahydrate ($Fe(NO_3)_3{\cdot}_9H_2O$) with melamine, aminotriazole, and aminoguanidine hydrochloride to form Fe/gC_3N_4, Fe/C_3N_5, and Fe/C_3N_6, respectively, with metal loading of 2 wt.%, which is recommended metal percentage from a previous work carried out by our group [42]. The typical pyrolysis was also carried out in N_2

atmosphere for 3 hours at the same aforementioned calcination temperatures and the collected samples were denoted as, Fe/gC_3N_4-M, Fe/C_3N_5-M, and Fe/C_3N_6-M (M for mechanical mixing). The preparation parameters of all samples were summarized in Table 3 in addition to Figure 3.3, which shows real pictures of the resulted phases.

3.3.3. Synthesis of Fe/gC_3N_4 by polymerization method

The catalyst was prepared by dispersing 1 gram of melamine in 30 mL of ethanol including $Fe(NO_3)_3{\cdot}_9H_2O$ with metal loading 2 wt.% which is recommended from a previous work carried out by our group [42]. Then, 60 mL of nitric acid (0.1 M) was dropped to the solution under stirring for 30 minutes at 25 °C. A yellowish precipitate was obtained and then washed by ethanol, and dried at 80 °C for 12 hours, followed by calcination at 550 °C for 3 hours in N_2 atmosphere (Figure 3.4). The synthesized catalyst was denoted as Fe/gC_3N_4-P (P for polymerization). In addition, The bimetallic catalyst FeTi/gC_3N_4-P was prepared by the same method but with metal loading of 1 wt.% of each Fe and Ti and the trimetallic catalyst FeTiCu/gC_3N_4-P was synthesized with metal loading of 0.66 wt.% of Fe, Ti, and Cu. Moreover, metal-free gC_3N_4 was synthesized by the same method but without Fe, Ti, or Cu precursors and a commercial palladium (Pd) catalyst supported on C with 20wt.% metal loading was purchased from Sigma Aldrich for comparison.

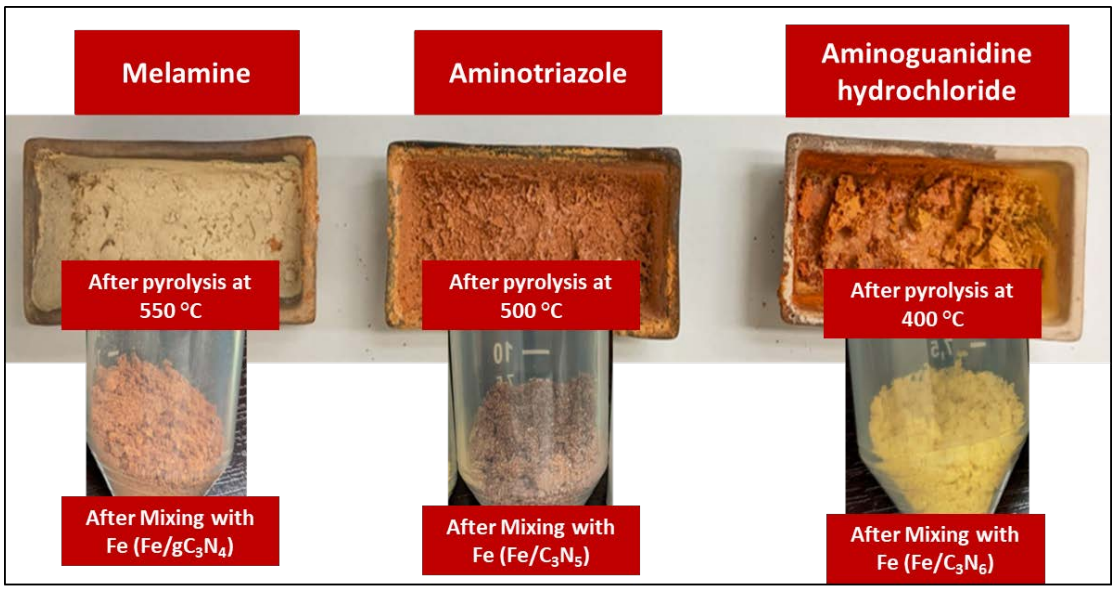

Figure 3.3. Real pictures of the prepared C_3N_x phases (upper side) and Fe/C_3N_x catalysts prepared by mechanical mixing.

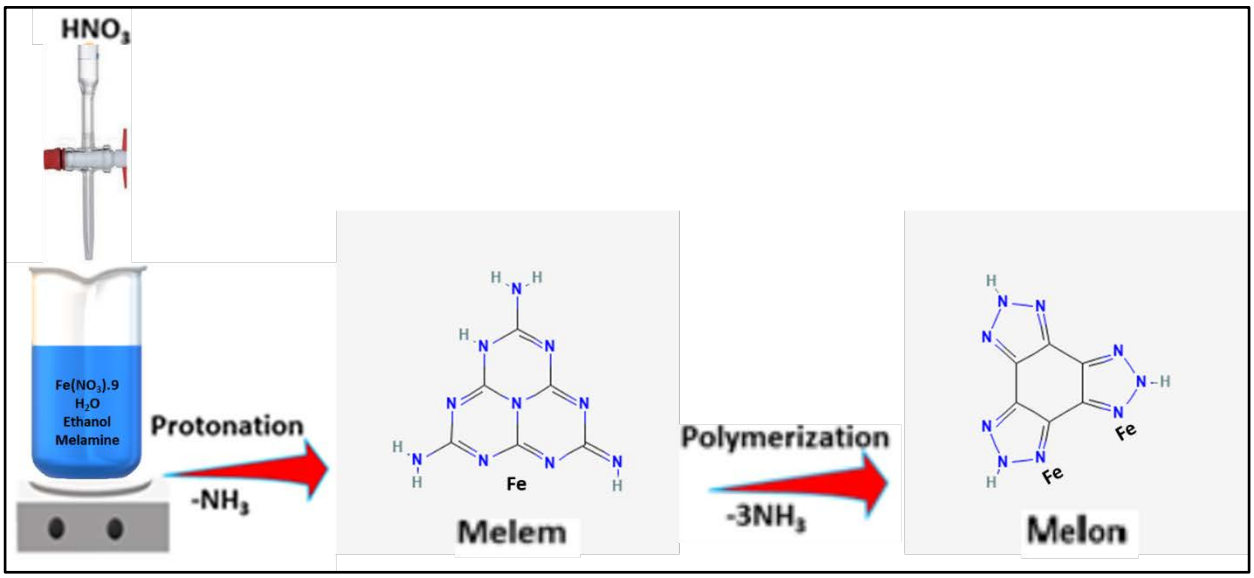

Figure 3.4. The proposed fabrication mechanism of Fe/gC_3N_4

Table 3.1 A summary of preparation conditions of the synthesized samples

Sample	**Preparation Method**	**Calcination Temperature (°C)**	**Fe Loading (wt.%)**	**Ti Loading (wt.%)**	**Cu Loading (wt.%)**
gC_3N_4	Pyrolysis	550	/	/	/
C_3N_5	Pyrolysis	500	/	/	/
C_3N_6	Pyrolysis	400	/	/	/
Fe/gC_3N_4	Mechanical Mixing then Pyrolysis	550	2	/	/
Fe/C_3N_5	Mechanical Mixing then Pyrolysis	500	2	/	/
Fe/C_3N_6	Mechanical Mixing then Pyrolysis	400	2	/	/
Fe/gC_3N_4	Polymerization	550	2	/	/
FeTi/ gC_3N_4	Polymerization	550	1	1	
FeTiCu/ gC_3N_4	Polymerization	550	0.66	0.66	0.66

3.4. Characterization Techniques

Characterization of catalysts is a crucial process in the field of catalysis, aimed at understanding their structure, composition, and activity. This analytical exploration provides insights into how catalysts facilitate and accelerate chemical reactions,

enabling the design of more efficient and selective catalytic processes. The characterization of the catalysts involves identifying their physical and chemical properties that can reveal how effectively they function in the reaction. The experimental techniques and their machines used for identifying and characterizing of all samples are mentioned as follows;

3.4.1 Scanning Electron Microscopy (SEM)

This analysis was used to provide us with high-resolution imaging for exploring the morphology of the synthesized catalysts (Nova Nano SEM 450 and Quanta 200 SEM).

3.4.2 X-ray diffraction (XRD)

This technique was used to identify the crystallinity of the as-synthesized catalysts. The XRD analyses were carried out using desktop X-ray diffractometer (Rigaku,MiniFlexII) with a scanning speed of 4°/min.

3.4.3 Fourier-transform infrared spectroscopy (FTIR)

This analysis was also used to identify the organic and polymeric properties. The measurements were performed by Thermo Scientific Nicole iS 10 FTIR Spectrometer with Mid-infrared Ever-Glo and Tungsten/halogen source.

3.4.4 X-ray photoelectron spectrometer

This analysis is deployed for the elemental surface analyses and the surface chemical bonding of the prepared samples using AXIS Ultra DLD, KRATOS.

3.4.5 Specific surface area

This measurement was obtained via N_2 sorption experiments at liquid nitrogen by performing the Brunauer-Emmett-Teller (BET) analysis. In addition, the pore size measurements were performed using the Barret-Joyner-Halender method (BJH).

3.4.6 H_2-Temperature Programmed Reduction (H_2-TPR)

The analyses were carried out through (ChemiSorb-2750, Micrometrics). The process included two sages; firstly the pretreatment and then the analysis. 50 mg of the catalyst

was put in a quartz tube and the temperature was ramped up to 200 °C with a ramping rate of 10 °Cmin^{-1} in 25 ml^{-1}. of argon. After the samples were degassed for one hour, then cooled to 25 °C in the flow of Ar. The pretreatment was then followed by H_2-TPR analysis as 25 ml/min. of 10 vol.% of H_2 balanced in Ar was introduced to the sample while the temperature was raised up to 600 °C with a heating rate of 10 °Cmin^{-1}.

3.4.7 CO-Temperature programmed desorption (CO-TPD)

The analysis of the samples was carried out using the same aforementioned equipment (ChemiSorb-2750, Micrometrics) and the samples were also degassed using the same method for 1 h, then cooled to 25 °C in a Ar flow. The pretreatment was then followed by CO-TPD analysis. The sample temperature was set at 40 °C and then 25 ml/min. of 10 vol.% of CO balanced in Ar was introduced for 1 hour. Then, 25 ml/min. of pure Ar was introduced to the sample while the system temperature was increasing to 600 °C with a heating rate 10 °Cmin^{-1}.

3.4.8 Raman Analyses

The Raman analyses of samples were carried out using Thermo fisher scientific DXR Raman Microscope.

3.4.9 Thermal Gravimetric Analysis (TGA)

The TGA of the samples was done by the Perkin Elmer equipment at 25 to 800 °C and heating rate 10 °Cmin^{-1}.

Chapter 4

Exploring the catalytic properties of C_3N_x phases (x= 4, 5, 6)

4.1 Results and discussion

4.1.1 Characterization

The three phases, gC_3N_4, C_3N_5, and C_3N_6, obtained after pyrolysis of melamine, aminotriazole, and aminoguanidine hydrochloride, respectively, were characterized by various techniques. The FTIR analysis of the three phases (Figure 4.1a) confirmed the formation of the carbon nitride as the spectrum revealed an absorption band at 810 cm^{-1}, which is assigned to the the s-triazine unit [45, 46]. In addition, some obvious broad bands between 1100 and 1600 cm^{-1} are observed, which are attributed to the stretching mode of C-N [45, 46]. Besides, the bands appeared at around 3200 cm^{-1} are attributed to the N-H [47]. However, The FTIR analyses did not show clear differences among the three phases. The XRD analyses of gC_3N_4, C_3N_5, and C_3N_6 showed the main peak of carbon around 27.5 two theta, which is ascribed to the [002] facet (Figure 4.1b). In addition, another peak were observed around 12.9 two theta, which is ascribed to the carbon [100] [48]. Moreover, the gC_3N_4 showed sharper peaks than C_3N_5, which showed slightly sharper peaks than C_3N_6 indicating that gC_3N_4 is more crystallized than C_3N_5, which is might be slightly more crystallized than C_3N_6.

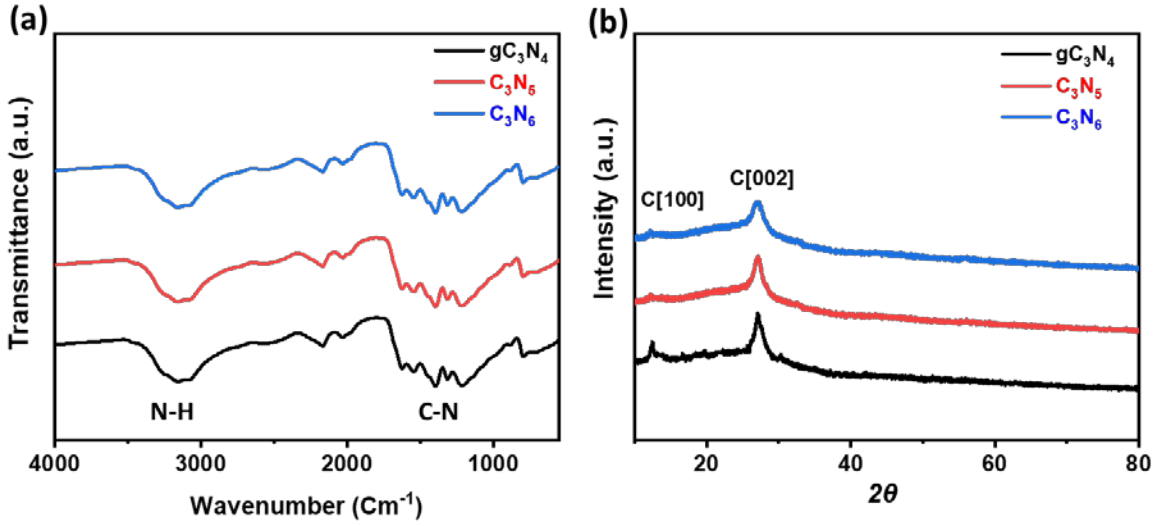

Figure 4.1 (a) FTIR and (b) XRD of the three C_3N_x phases.

In addition, the SEM analyses of the C_3N_x phases showed heterogeneous mixtures of large particles with various morphologies without unique or specific structures. The SEM did not show a unique morphology as all phases were prepared by the traditional pyrolysis without any modifications (Figures 4.2a-c). In addition, the EDX analysis approved the existence of C and N in all phases indicating the successful preparation (Figure 4.2d). The EDX analyses showed that C and N content of gC_3N_4 was 32.42 and 63.37 wt%, respectively, and C and N of C_3N_5 was 31.78 and 65.04 wt%, respectively. Besides, C and N of C_3N_6 was 28.92 and 65.54 wt%, which matches with the trend of increasing the nitrogen atoms in the phases.

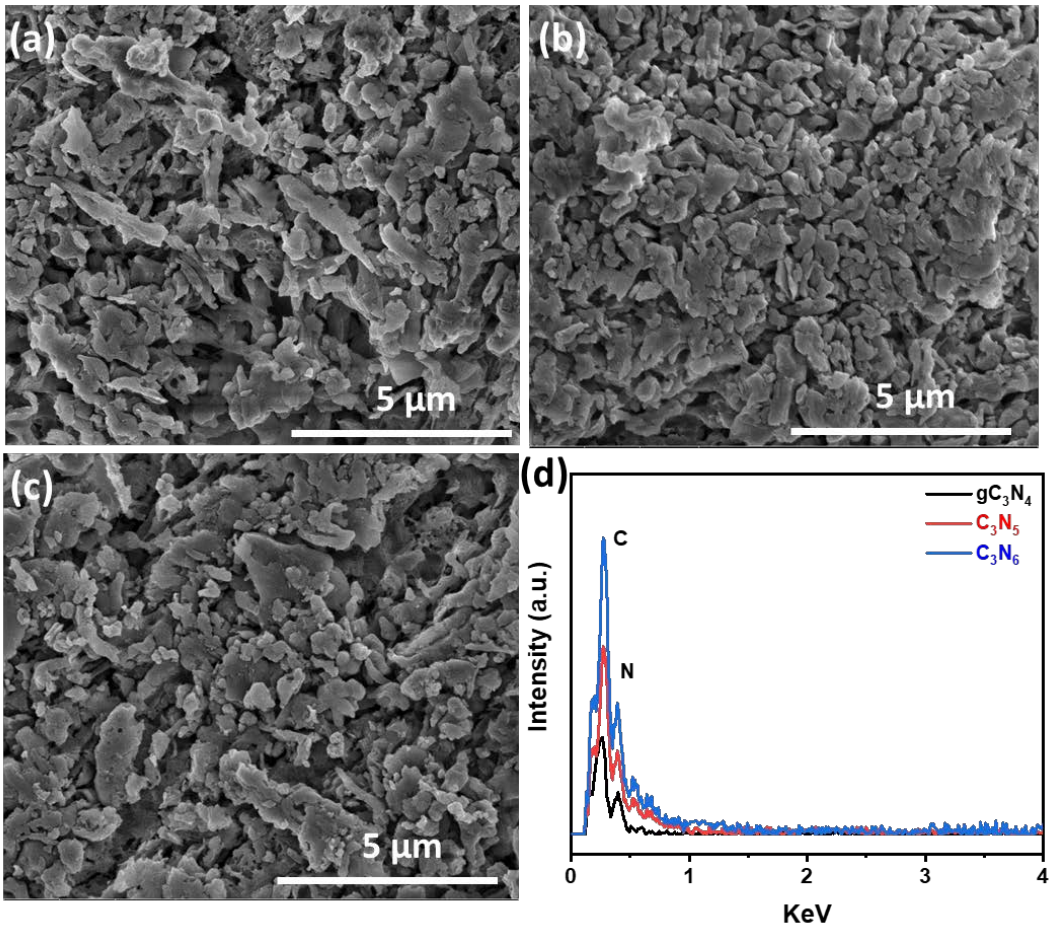

Figure 4.2 SEM images of (a) gC_3N_4, (b) C_3N_5, (d) C_3N_6, and (d) EDX analysis of the three C_3N_x phases.

The XPS full surface survey of gC_3N_4, C_3N_5, and C_3N_6 (Figure 4.3a) confirmed the successful preparation of the three phases as the spectra of C1s and N1s were observed in all phases in addition to O1s, which is surface oxygen can not be avoided by the machine. In addition, the surface survey showed that the atomic concentration of C and N in gC_3N_4 was 38.36 and 59.43, respectively, and in C_3N_5 was 38.07 and 60.73, respectively. Besides, the atomic concentration of C and N in C_3N_6 was 38.01 and 61.14, which matches with the trend of increasing the N atoms in the three phases. Moreover, the high-resolution C1s spectra included two fitted peaks; the first one at 284.3 eV, ascribed to the C-C bond and the second peak at 286.27 eV, assigned to the

carbon atoms bonded to three nitrogen atoms (Figures 4.3b-c) [49]. Moreover, the high-resolution C1s spectra of C_3N_6 showed higher shift in the binding energy than C_3N_5, which showed a higher shift than gC_3N_4. That difference of binding energies of the C_3N_x phases is attributed to the additional nitrogen atoms in C_3N_5, and C_3N_6, which increases the electronegativity and can attract the electrons towards their self [50], and accordingly, increasing the nitrogen atoms increases the binding energy [51, 52]. In addition, the high-resolution N1s spectra confirmed the C1s result showing a slight higher shift with the same trend. The fitted peaks of the high-resolution N1s spectra showed the existence of three distinguishable nitrogen environments (Figure 4.3d-e), which are corresponded to the pyridinc, pyrrolic, and graphitic N species existed in the C_3N_x phases [53].

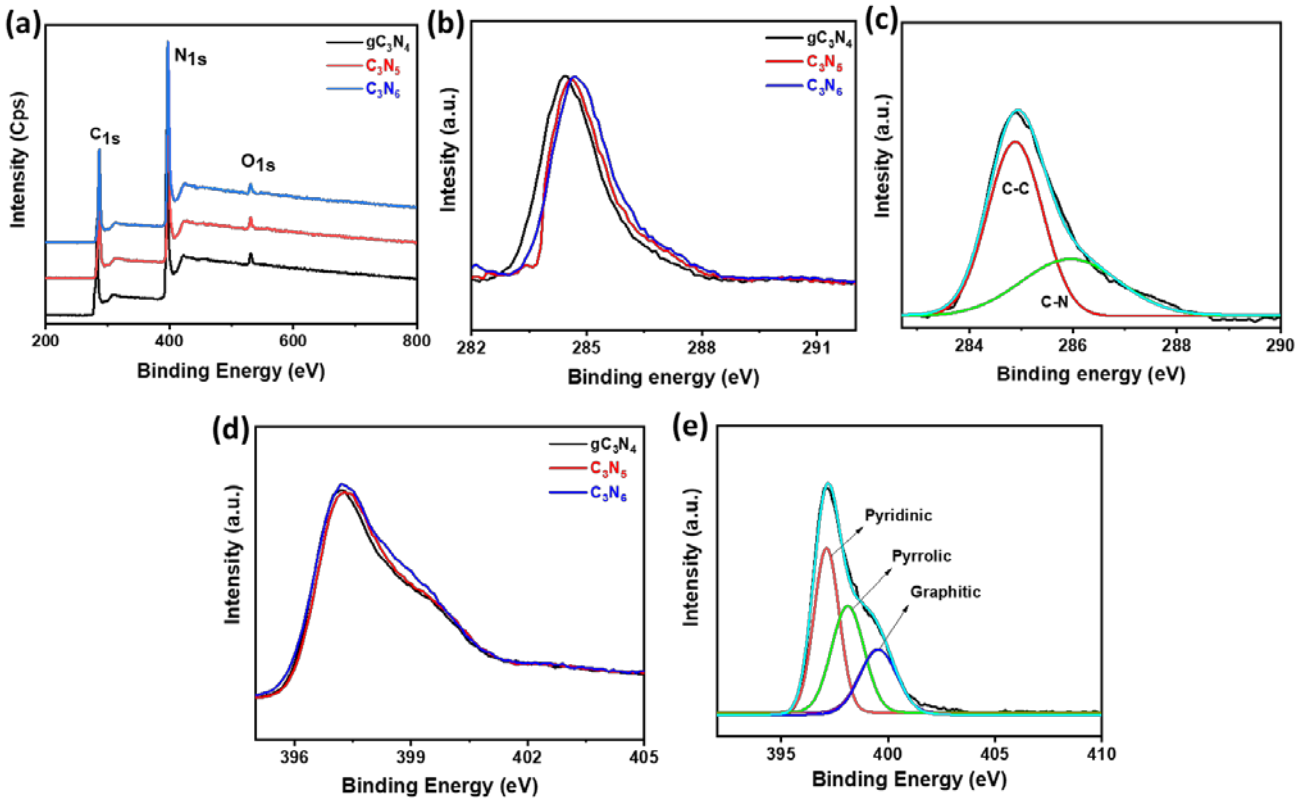

Figure 4.3. (a) XPS-Full surface Survey, (b-c) High-resolution C1s XPS spectra and its interpretation, and (d-e) high-resolution N1s XPS spectra and its interpretation of gC_3N_4, C_3N_5, and C_3N_6.

The thermogravimetric analysis (TGA) was carried out under air to explore the thermal stability of the C_3N_x phases and the results showed a significant difference in the thermal stability of each phase (Figure 4.4a). The gC_3N_4 showed the highest thermal stable behavior, as it was robust up to 600 °C without any instability and then started a slight weight loss till 650 °C, which indicates the beginning of the oxidation. Finally, the sharp weight loss occurred at 650 to 750 °C, which indicated the complete oxidation of carbon to carbon dioxide [54]. On the other hand, C_3N_5 and C_3N_6 showed less stable behavior as they started to lose weight around 500 °C indicating a slight oxidation between 500 and 550 °C and then started the sharp weight loss after 550 °C until 610 °C, where the complete oxidation of carbon occurred. Similar results have been reported previously [55]. That higher stable behavior of gC_3N_4 might be attributed to the higher crystallinity, indicated by XRD.

The Raman analysis of the C_3N_x phases (Figure 4.4b) showed a broad peak in the range of 1200 to 1700 cm^{-1}, representing a combination of the D and G bands of carbon. In addition, the Raman spectrum showed an additional broad peak (2D band), which is a Raman signature for the sp2 materials [56]. However, the Raman analysis did not show differences among the three phases. In addition, the CHNSO analysis showed that the gC_3N_4, C_3N_5, and C_3N_6 have a carbon wt.% of 36.49, 36.12, and 36.06, respectively, and nitrogen wt.% 62.08, 62.16, and 62.19, respectively (Table 4.1), which matches with other reported results [47]. There was a slight increase in the nitrogen content synchronizing with a decrease in the carbon content, which matches with the trend of nitrogen increasing in the three phases and confirms the EDX results. In addition, little amounts of hydrogen were detected, indicating the presence of N-H bonding, which was observed earlier by the FTIR.

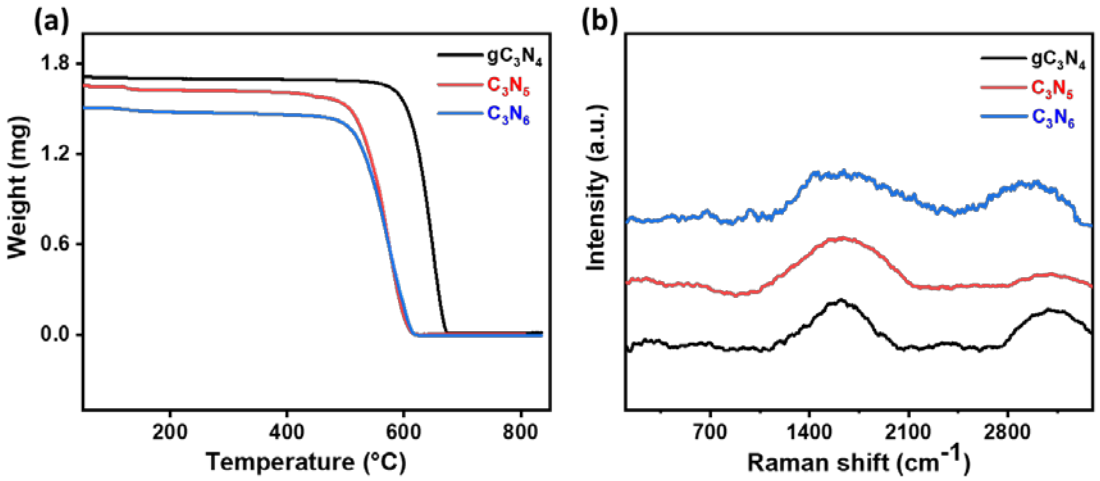

Figure 4.4 (a) TGA and (b) Raman analysis of C_3N_4, C_3N_5, and C_3N_6.

Table 4.1 CHNSO analysis of the C_3N_x phases.

Sample	**C (wt.%)**	**N (wt.%)**	**H_2 (wt.%)**
gC_3N_4	36.49	62.08	1.43
C_3N_5	36.12	62.16	1.72
C_3N_6	36.06	62.19	1.75

4.1.2. Catalytic Tests

All prepared C_3N_x phases; gC_3N_4, C_3N_5, and C_3N_6 were tested in the aforementioned system that is illustrated in chapter 3.2. (Figure 3.1). at the atmospheric pressure and at operating temperatures ranging from room temperature up to 400 °C. The metal-free C_3N_x phases did not show any catalytic activity for the CO oxidation reactions (Figure A3).

4.2. Conclusions

FTIR, XPS, and EDX analyses confirmed the successful preparation of gC_3N_4, C_3N_5, and C_3N_6. In addition, the XPS analysis showed an indication to the higher content of nitrogen in C_3N_5 and C_3N_6. In addition, the XRD analysis showed that gC_3N_4 owned sharper carbon peaks than the ones of C_3N_5 and C_3N_6, which indicates that gC_3N_4 is more crystalized than C_3N_5 and C_3N_6. Moreover, the TGA showed a significant difference among the three C_3N_x phases as the gC_3N_4 was more thermally stable than C_3N_5 and C_3N_6, which is attributed to its higher crystallinity. The gC_3N_4 was robust up to 600 °C without any instability and then started a slight weight loss until 650 °C, which indicates the beginning of the oxidation. Finally, the sharp weight loss occurred at 650 to 750 °C, which indicates the complete oxidation of carbon to carbon dioxide. C_3N_5 and C_3N_6 showed less stable behavior, as they started to lose weight around 500 °C, indicating a slight oxidation between 500 and 550 °C and then started the sharp weight loss after 550 °C until 610 °C, where the complete oxidation of carbon occurred. Furthermore, the CHNSO analyses confirmed the carbon and nitrogen contents of all samples with the increasing trend of nitrogen atoms in the three phases.

Chapter 5

Catalytic performance of Fe-doped catalysts; Fe/gC_3N_4, Fe/C_3N_5, and Fe/C_3N_6

5.1 Results and discussion

5.1.1. Characterization

The Fe/gC_3N_4-M, Fe/C_3N_5-M, and Fe/C_3N_6-M were prepared by the mechanical mixing method as mentioned earlier in chapter 3 and then they were characterized by different techniques to explore and evaluate them. The FTIR analyses of the three catalysts (Figure 5.1a) approved again the formation of the carbon nitride as the spectrum showed the absorption band at 810 cm^{-1}, attributed to the s-triazine unit and the broad bands between 1100 and 1600 cm^{-1}, ascribed to the stretching mode of C-N in addition to the bands around 3200 cm^{-1} of the N-H. Similarly observations were previously reported for the functional groups [45, 46]. Also, the FTIR analyses did not provide a significant difference for differentiation among the catalysts (Figure 5.1b). This matches with the FTIR analysis of the metal-free phases, as the spectrum revealed an absorption band at 810 cm^{-1}, assigned to the the s-triazine unit [45, 46]. In addition, some obvious broad bands between 1100 and 1600 cm^{-1} are observed, attributed to the stretching mode of C-N [45, 46]. Besides, the bands appeared at around 3200 cm^{-1} are attributed to the N-H [47].

The XRD analysis of the catalysts Fe/gC_3N_4-M, Fe/C_3N_5-M, and Fe/C_3N_6-M displayed the main peak of carbon at around 27.6 two theta, attributed to the [002] facet besides the peak at 12.9 two theta, assigned to C [100] (Figure 5.1c) [48]. Moreover, Fe/gC_3N_4-M showed sharper carbon peaks than Fe/C_3N_5-M and Fe/C_3N_6-M, which confirmed that gC_3N_4 is more crystalized than C_3N_5 and C_3N_6 as observed before. This

is also matches with the XRD analyses of the metal-free phases that showed the main peak of carbon around 27.5 two theta, ascribed to the [002] facet and another peak around 12.9 two theta, ascribed to the carbon [100] [48]. Moreover, gC_3N_4 showed sharper peaks than C_3N_5, which showed slightly sharper peaks than C_3N_6, indicating that gC_3N_4 is more crystallized than C_3N_5, which is slightly more crystallized than C_3N_6. Furthermore, the XRD analyses of all samples showed a clear difference between the metal-free C_3N_x phases and the Fe-doped ones, as Fe/gC_3N_4-M, Fe/C_3N_5-M, and Fe/C_3N_6-M showed sharper peaks, which indicates increasing of crystallinity caused by Fe addition (Figure 5.1d). The Fe enhanced the crystallinity of the C_3N_x phases, which is attributed to the successful insertion of Fe to the crystal lattice causing lattice distortion [57, 58]. However, the XRD could not detect the Fe peaks, which is attributed to its low concentrations in the catalysts.

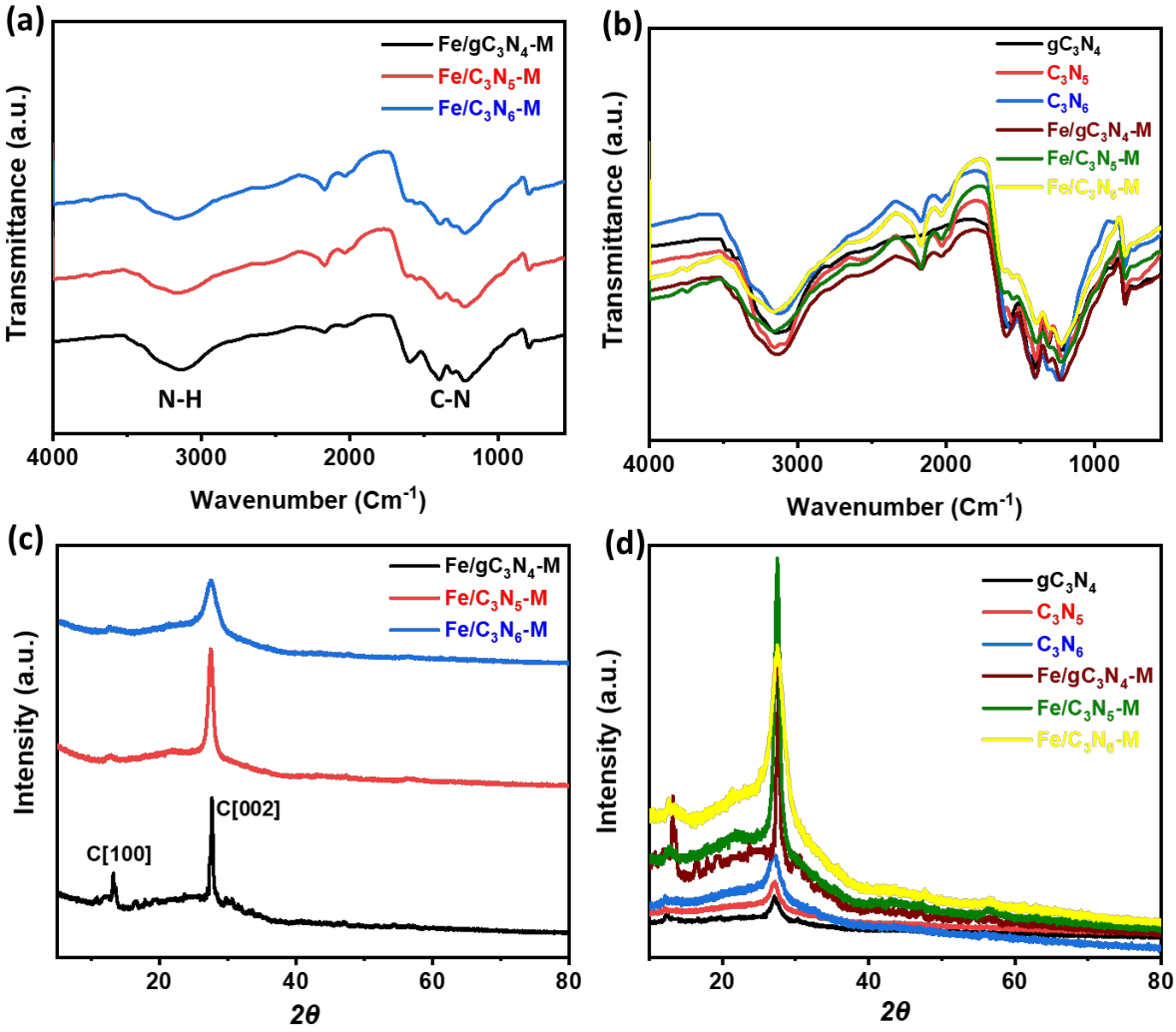

Figure 5.1. The FTIR analyses of the catalysts Fe/C_3N_x (a) and the C_3N_x phases (b), and the XRD analyses of the catalysts Fe/C_3N_x (c) and the C_3N_x phases (d).

The SEM analyses of the three catalysts (Figures 5.2 a-c) showed bulk images of heterogeneous mixtures of large particles with various morphologies without unique or specific structures, without contributing much to the differences among the as-synthesized catalysts. However, the EDX profiles confirmed the existence of iron in the three catalysts (Figure 5.2d) with approximately 2% of iron in each catalyst.

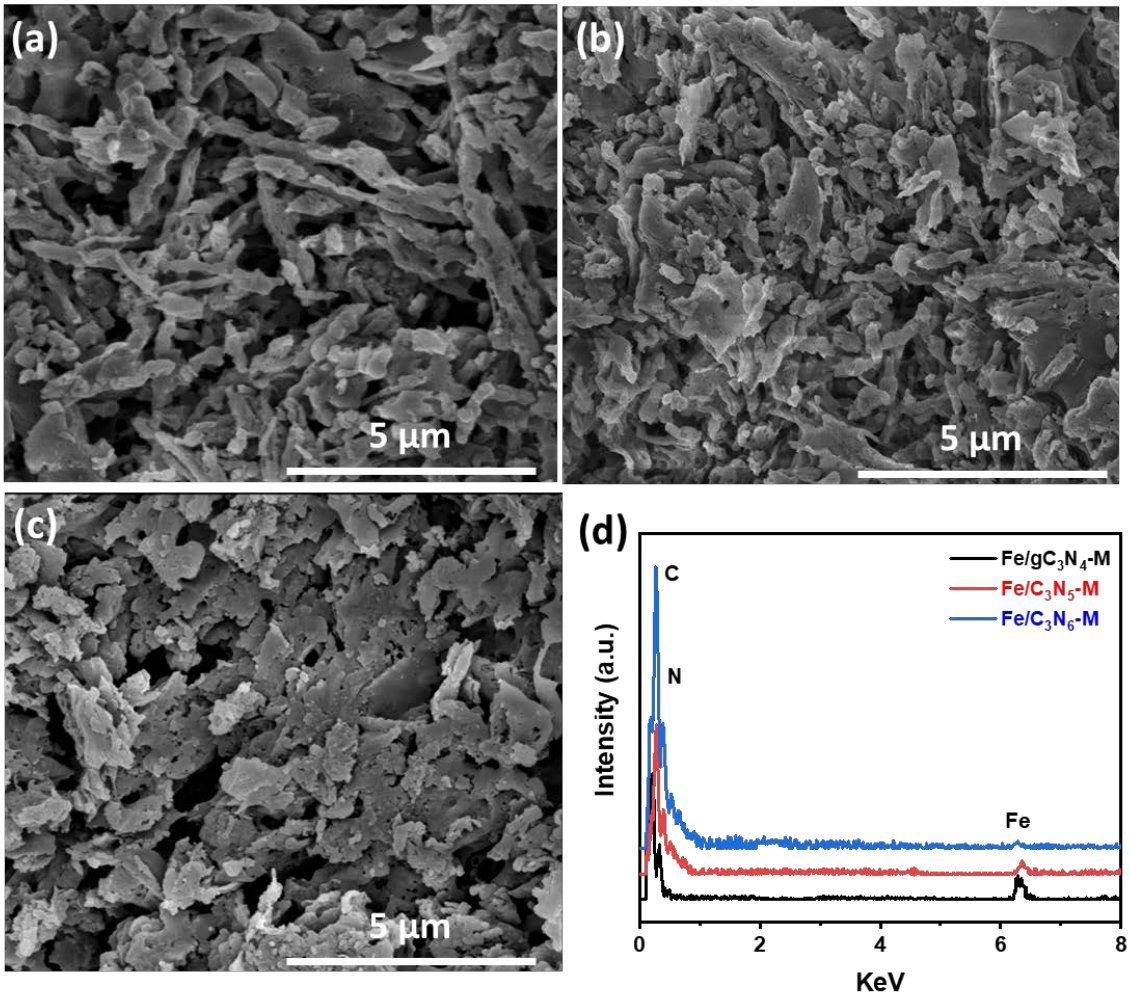

Figure 5.2. The SEM images of (a) Fe/gC_3N_4-M, (b), Fe/C_3N_5-M, (c) Fe/C_3N_6-M, and (d) the EDX of all of them.

The XPS full surface survey confirmed the presence of Fe2p in addition to C1s, N1s, and O1s, which is surface oxygen can not be avoided by the machine (Figure 5.3a). The high-resolution C1s spectra and N1s spectra confirmed the successful preparation as previously discussed in chapter 4 [49]. In addition, the high-resolution C1s spectra of Fe/C_3N_6-M showed higher shift than Fe/C_3N_5-M and Fe/gC_3N_4-M (Figures 5.3b-c), which is attributed to the additional nitrogen atoms[51, 52] as discussed in chapter 4. In addition, the fitted peaks of the high-resolution N1s spectra showed the presence of three nitrogen environments (Figures 5.3d-e), attributed to the pyridinc, pyrrolic, and graphitic N species [53]. Moreover, the high-resolution spectra of Fe2p regions showed

a peak at ~708 eV, which is ascribed to Fe2p3/2 and another peak at ~723 eV, which is ascribed to Fe2p1/2 (Figure 5.3 f-g) [59]. The fitted peaks of Fe2p indicated that the main phase of the iron is the metallic phase (Fe^0), and the other fitted small peaks, ascribed to the FeO and Fe_2O_3 might be formed only on the surface due to the surface oxygen. The Fe addition did not affect the peaks' position, which might be due to the low concentration of Fe compared to C and N concentrations.

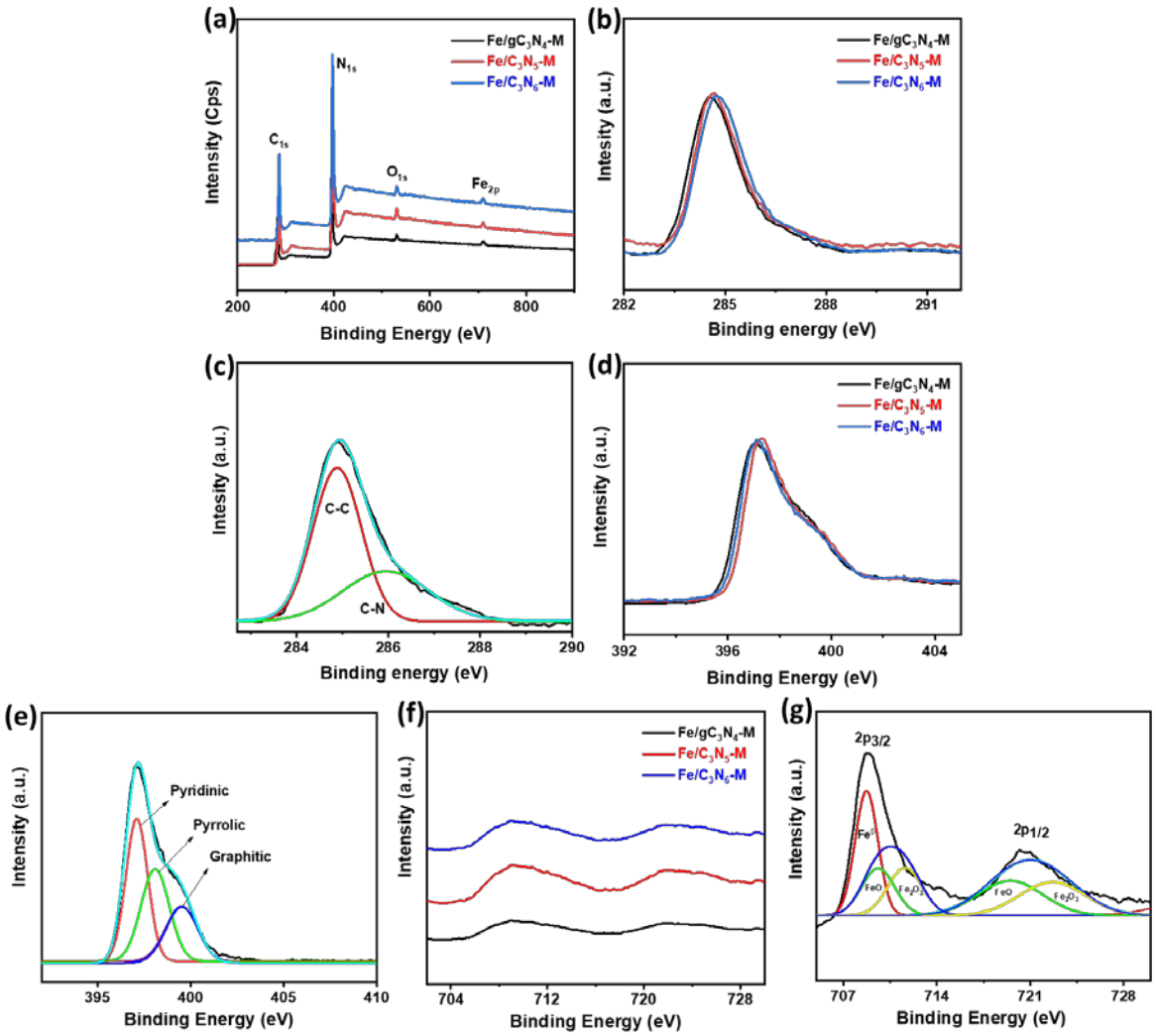

Figure 5.3. XPS Full surface Survey (a), High-resolution C1s spectra and its interpretation (b-c), high-resolution N1s spectra and its interpretation (d-e), and high-resolution spectra of Fe2p (f-g) of Fe/gC_3N_4-M, Fe/C_3N_5-M, and Fe/C_3N_6-M.

Interestingly, The TGA analyses of Fe/gC_3N_4-M, Fe/C_3N_5-M, and Fe/C_3N_6-M showed an evidence for the effect of Fe addition (Figure 5.4a), which increased the thermal stability of the three phases matching with the results reported in the literature [60, 61]. The complete decomposition, which represent the complete oxidation of carbon of Fe/gC_3N_4-M was enhanced to achieve 780 °C instead of 680 °C and the complete decomposition of Fe/C_3N_5-M and Fe/C_3N_6-M were improved from 610 °C to reach about 700 °C and 750 °C, respectively. Moreover, start of decomposition, representing the beginning of carbon oxidation, of the three catalysts was increased by around 20 °C for each. Fe/gC_3N_4-M started the decomposition after 600 °C and continued till 780 °C, which is superior to Fe/C_3N_5-M and Fe/C_3N_6-M (Figure 5.4b), which is attributed to the higher thermal stability of the gC_3N_4 phase and the enhanced effect of iron [60, 61].

In addition, Raman analyses presented an obvious difference between the C_3N_x supports (gC_3N_4, C_3N_5, and C_3N_6) and their catalysts, as Fe/gC_3N_4-M, Fe/C_3N_5-M, and Fe/C_3N_6-M showed a separated D band peak around 1350 cm^{-1}, representing the disordered carbon, and G band peak around 1582 cm^{-1}, corresponded to the graphitic carbon (Figure 5.4c). That result indicates that Fe also enhanced the graphitization of the C_3N_x phases strongly, which matches with the reported results [62, 63]. Moreover, the Raman spectra exhibited that ratio of ID/IG of Fe/gC_3N_4 was 0.87 but ID/IG of Fe/C_3N_5 and Fe/C_3N_6 were 1.010 and 1.015, which confirms that Fe/gC_3N_4 has mainly the graphitic carbon phase (Figure 5.4d). The 2D band was existed in all samples, which is Raman signature for the sp^2 materials [56]. In addition, the CHNSO analysis showed an increasing trend in nitrogen amounts in the three catalysts, indicating the presence of the additional nitrogen atoms of C_3N_5 and C_3N_6. Moreover, the CHNSO analysis showed a slight decrease in the concentration of C and N in the three catalysts compared to their concentrations in the metal-free phases (Table 5.1), which indicates

the Fe existence. In addition, small amounts of hydrogen were detected, indicating the presence of N-H bonding, which was observed previously by the FTIR.

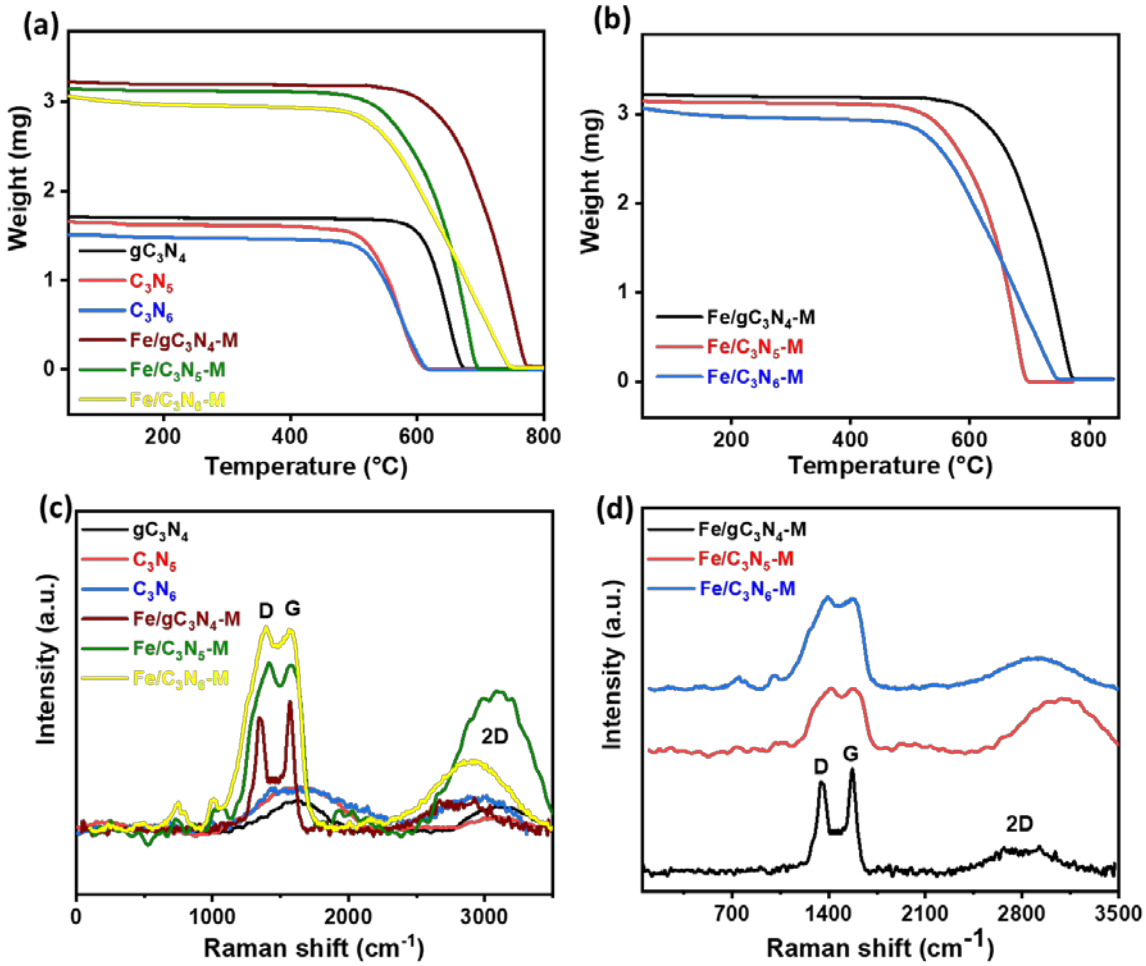

Figure 5.4. (a) TGA of C_3N_x phases and their catalysts, (b) TGA of Fe/gC_3N_4-M, Fe/C_3N_5-M, and Fe/C_3N_6-M, (c) Raman analyses of CN phases and their catalysts, and (d) Raman analyses of Fe/gC_3N_4, Fe/C_3N_5, and Fe/C_3N_6.

Table 5.1. CHNSO analysis of the Fe/CN catalysts.

Sample	**C (wt.%)**	**N (wt.%)**	**H_2 (wt.%)**
Fe/gC_3N_4	34.86	61.26	1.88

Fe/C_3N_5	34.45	61.57	1.94
Fe/C_3N_6	34.24	61.89	1.99

5.2. Catalytic Tests

The prepared C_3N_x-based catalysts; Fe/gC_3N_4-M, Fe/C_3N_5-M, and Fe/C_3N_6-M were tested in the previously illustrated reactor at operating temperatures up to 400 °C. Fe/gC_3N_4-M achieved the complete CO conversion at 291 °C, which was superior to Fe/C_3N_5-M, and Fe/C_3N_6-M that achieved the T_{100} (full CO conversion) at 322 °C and 335 °C, respectively (Figure 5.5a), which is attributed to the high crystallinity, graphitization, and thermal stability of Fe/gC_3N_4-M, as confirmed earlier. In addition, the reaction kinetics at low CO conversion of Fe/gC_3N_4-M was faster than that of Fe/C_3N_5-M, and Fe/C_3N_6-M, as shown in Figure 5.5b. Although Fe/gC_3N_4-M presented a considerable catalytic activity (T_{100} 291 °C) compared to some reported Fe-based catalysts (T_{100} 300 °C) [21], other reported Fe-based catalysts could achieve the full conversion at 255 °C only [64]. Thus, we optimized the catalyst using a recent unique polymerization method, which was developed by our group as explained in chapter 3 [42].

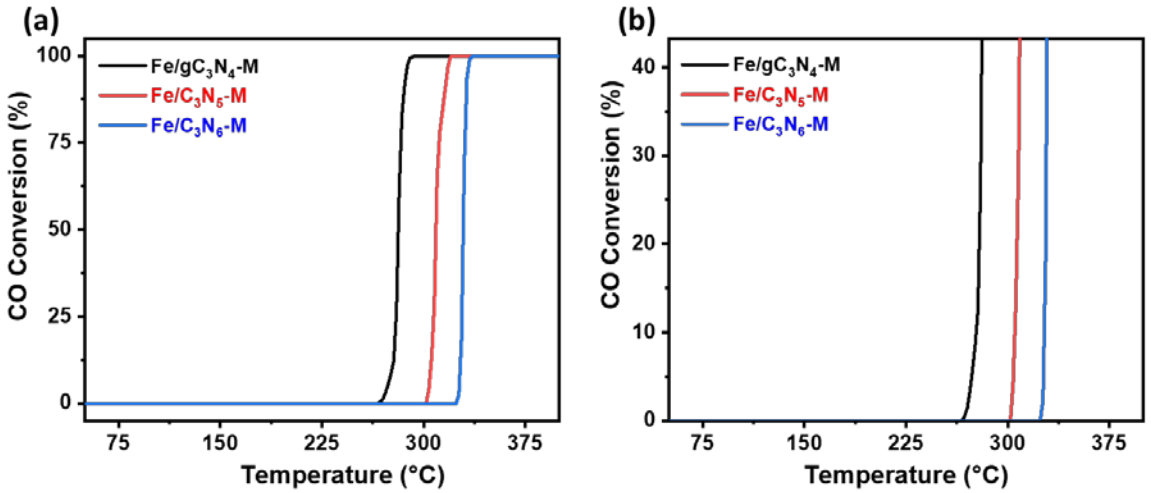

Figure 5.5 (a) Catalytic activity and (b) reaction kinetics of Fe/gC_3N_4-M, Fe/C_3N_5-M, and Fe/C_3N_6-M.

5.3. Conclusions

FTIR, EDX and XPS analyses indicated the successful preparation of the C_3N_x based catalysts; Fe/gC_3N_4-M, Fe/C_3N_5-M, and Fe/C_3N_6-M. In addition, the XPS analysis showed an indication to the higher content of nitrogen in Fe/C_3N_5-M, and Fe/C_3N_6-M. Moreover, XRD analyses indicated that Fe addition increased the crystallinity of the supports; gC_3N_4, C_3N_5, and gC_3N_6, and showed that Fe/gC_3N_4-M is more crystalized than Fe/C_3N_5-M and FeC_3N_6-M, which matches with the aforementioned XRD results of gC_3N_4, C_3N_5, and C_3N_6. The TGA showed an obvious increase in thermal stability of gC_3N_4, C_3N_5, and C_3N_6 after addition of Fe and confirmed that Fe/gC_3N_4-M is more thermally stable than Fe/C_3N_5-M and FeC_3N_6-M, which matches with the aforementioned TGA results of gC_3N_4, C_3N_5, and C_3N_6. Furthermore, Raman analyses showed the significant effect of Fe, which increased clearly the graphitization of the three catalysts and mainly the Fe/gC_3N_4-M, which showed higher graphitization than Fe/C_3N_5-M, and Fe/C_3N_6-M. Accordingly, the best catalytic properties of Fe/gC_3N_4-M led to the highest catalytic activity as it could achieve the complete CO conversion at 291 °C superior to Fe/C_3N_5-M (T_{100} 322 °C) and Fe/C_3N_6-M (T_{100} 335 °C), which is attributed to the high crystallinity and graphitization of gC_3N_4 phase. Those results explain why gC_3N_4 is the most reported phase generally and the only reported phase for the thermal CO oxidation. Thus, the subsequent study will be done with only gC_3N_4 phase.

Chapter 6

Catalytic performance of Fe/gC_3N_4-M prepared by mechanical mixing and Fe/gC_3N_4-P synthesized by the polymerization method

6.1 Results and discussion

Firstly, Fe/gC_3N_4-P catalyst was synthesized by the polymerization of melamine by nitric acid in the presence of ethanol, which includes the iron precursor followed by calcination at 550 °C as explained previously in chapter 3. This unique method allows the formation of hierarchical porous structures, which provides high surface area, eases the electron transfer, and enhances the atomic utilization [42]. The prepared catalyst denoted as Fe/gC_3N_4-P to be compared to the previously prepared one by mechanical mixing, which denoted as Fe/gC_3N_4-M.

6.1.1 Characterization

The FTIR analyses confirmed the successful fabrication of carbon nitride as previously discussed but without contribution to the differences between Fe/gC_3N_4-M and Fe/gC_3N_4-P, as the spectra of both was almost similar (Figure 6.1a). The XRD showed that Fe/gC_3N_4-P offered less crystallinity than Fe/gC_3N_4-M, as the main peak of C [002] was slightly shifted to lower two theta with more broadening than the peak of Fe/gC_3N_4-M in addition to disappearing of the peak of C [100] (Figure 6.1b), which is an indication for less crystallinity. This less crystallinity is occurred due to the addition of nitric acid used in the polymerization method, which can negatively affect the crystallinity[65]. In addition, the EDX analysis confirmed the presence of Fe in the Fe/gC_3N_4-P with approximately 1.87 wt% (Figure 6.1c) and the SEM

images interestingly showed the morphological difference of the two catalysts as Fe/gC_3N_4-M showed heterogeneous mixture of large particles with various morphologies without a unique or specific structure (Figure 6.1d). Fe/gC_3N_4-P showed unique hierarchical porous structures at different magnifications (Figures 6.1e-h). Those hierarchical porous structures are formed during the synthesis due to the release of NH_3 groups, caused by protonation of melamine by nitric acid [42]. This hierarchical porous structure is the main reason for the high catalytic performance as they can offer high surface area with active sites cavities in addition to easing the electron transfer and maximizing the atomic utilization.

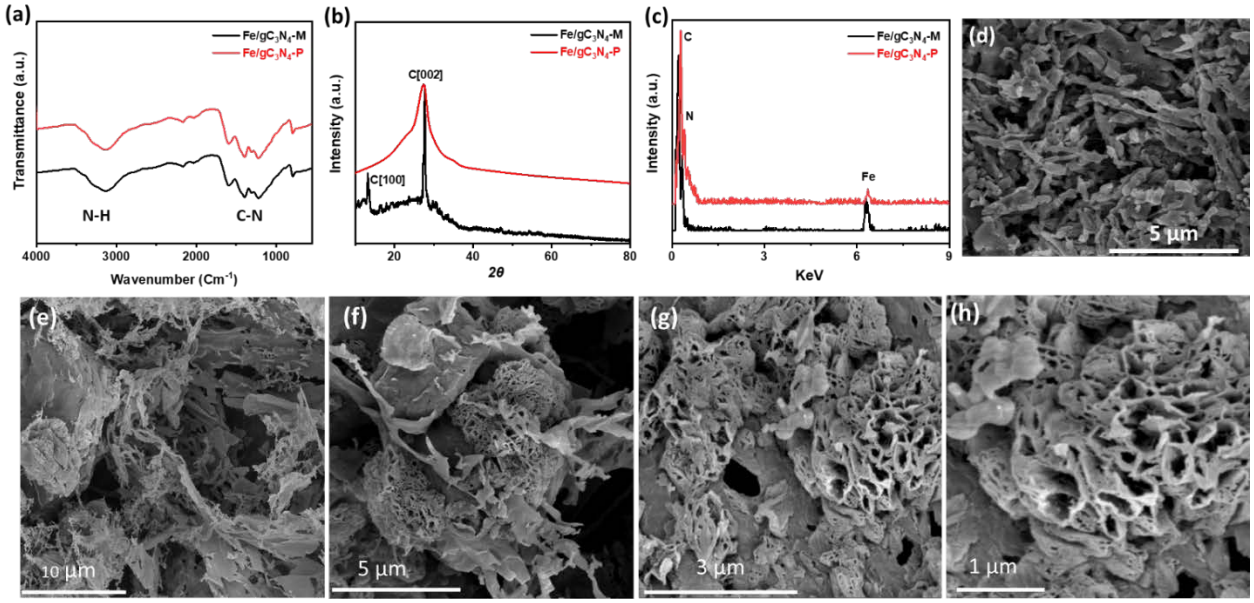

Figure 6.1. (a) FTIR, (b) XRD, and (c) (EDX) of Fe/gC_3N_4-M and Fe/gC_3N_4-P.

SEM images of Fe/gC_3N_4-M (d) and Fe/gC_3N_4-P (e-h).

In addition, the BET surface area measurements showed another significant difference as Fe/gC_3N_4-P offered 219.51 m^2/g, which is far higher than that of Fe/gC_3N_4-M (77.22 m^2/g) and all other C_3N_x phases and their catalysts (Table 6.1), which is attributed to the unique synthesis method. In addition, the N_2 adsorption-desorption isotherms of Fe/gC_3N_4-P (Figure 6.2a) showed the isotherm of an H4 hysteresis loop near to the

type-IV curve with the highest adsorption comprising two stages capillary condensation at 0.5 ≤ P/Po ≤ 0.9, which indicates the trimodal pore size distribution containing micro-, meso- and macro-porous[66], which was not observed in the N_2 adsorption-desorption isotherms of Fe/gC_3N_4-M (Figure 6.2b). Moreover, the pore size distribution calculated using Barrett-Joyner-Halenda method (BJH) confirmed the existence of multiple pores with average diameter ranging from 5 to 90 nm (Figure 6.2c). The XPS full surface survey confirmed the presence of Fe (Figure 6.2d). However, the high-resolution spectra of C1s, N1s and Fe2p did not show a clear difference between the Fe/gC_3N_4-M and Fe/gC_3N_4-P (Figures 6.2e-g).

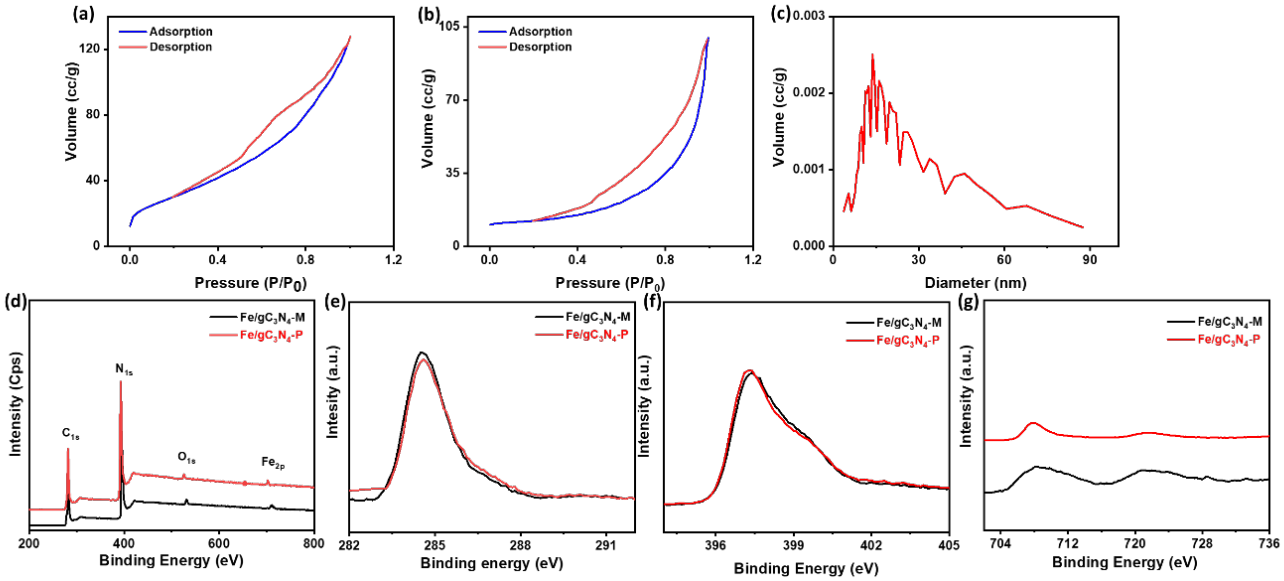

Figure 6.2 N_2 isotherms of (a) Fe/gC_3N_4-P and (b) Fe/gC_3N_4-M, (c) pore size distribution of Fe/gC_3N_4-P, (d) XPS full surface survey of Fe/gC_3N_4-M and Fe/gC_3N_4-P, (e) C1s spectra, (f) N1s spectra, and (g) Fe2p spectra of Fe/gC_3N_4-P.

In addition, the TGA analyses of Fe/gC_3N_4-M and Fe/gC_3N_4-P (Figure 6.3a) did not differentiate between the two catalysts and showed the aforementioned stable behavior as they stay stable up to 600 °C and then start a slight weight loss, representing the beginning of carbon oxidation, till 650 °C and finally the sharp decomposition until

780 °C, where the complete conversion of carbon to carbon dioxide occurred. Besides, the Raman spectrum (Figure 6.3b) of Fe/gC_3N_4-P presented a slight higher I_D/I_G ratio (0.93), which is more than that of Fe/gC_3N_4-M (0.87), which might be a hint for less graphitization caused by the polymerization method.

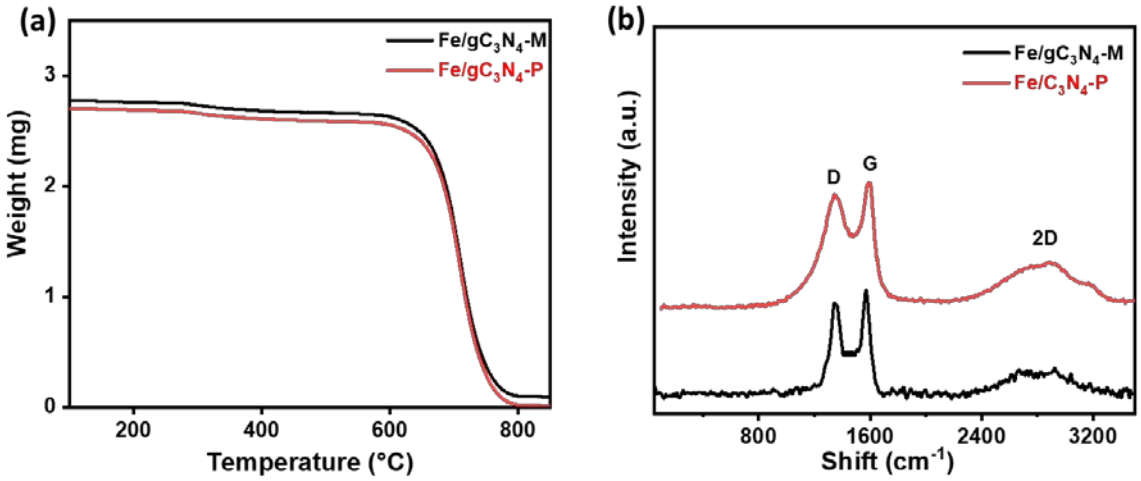

Figure 6.3. (a) TGA, (b) Raman of Fe/gC_3N_4-M and Fe/gC_3N_4-P

Table 6.1 BET surface area measurements of all samples.

Sample	**BET (m^2/g)**
gC_3N_4	82.86
C_3N_5	73.34
C_3N_6	79.12
Fe/gC_3N_4-M	77.22
Fe/C_3N_5-M	86.46
Fe/C_3N_6-M	75.12
Fe/gC_3N_4-P	219.51
FeTi/gC_3N_4-P	226.46
FeTiCu/gC_3N_4-P	215.12

6.1.2. Catalytic Tests

The catalytic activity tests were carried out at operating temperatures range of 25 to 300 °C at the aforementioned reactor (Chapter 3). The catalyst Fe/gC_3N_4-P presented higher catalytic activity than Fe/gC_3N_4-M, as it could achieve the T_{100} at 245 °C, while Fe/gC_3N_4-M achieved it at 291 °C, as shown in Figure 6.4a. This is attributed to the high surface area and the porous structure of the Fe/gC_3N_4-P that enhance the electron transfer, improve the active sites cavities, and maximize the atomic utilization. Besides, the reaction kinetics of the Fe/gC_3N_4-P at low CO conversion were far faster than that of Fe/gC_3N_4-M as seen in Figure 6.4a.

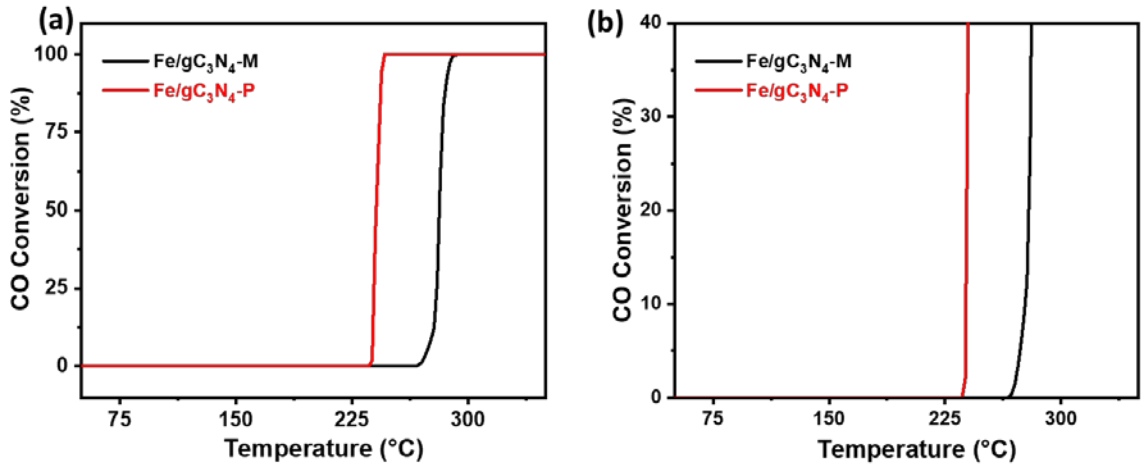

Figure 6.4. (a) Catalytic activity tests and (b) kinetic reactions of Fe/gC_3N_4-M and Fe/gC_3N_4-P

6.2. Conclusions

- FTIR, EDX, and XPS analyses confirmed the successful preparation of Fe/gC_3N_4-P, which prepared by the polymerization method. In addition, the XRD analysis showed that Fe/gC_3N_4-P offered less crystallinity than Fe/gC_3N_4-M and also the Raman analysis indicated less graphitization, which is might be caused by the deployed polymerization method. The SEM images showed the formed hierarchical porous

structure of Fe/gC_3N_4-P and the BET surface area measurements of Fe/gC_3N_4-P showed 219 m^2/g, which was far higher than Fe/gC_3N_4-M (77 m^2/g), which is attributed to the polymerization method. In addition, The catalytic activity of Fe/gC_3N_4-P was higher than that of Fe/gC_3N_4-M as Fe/gC_3N_4-P achieved the complete CO conversion at 245 °C, while Fe/gC_3N_4-M achieved it at 291 °C, ascribed to the high surface area and the porous structure of Fe/gC_3N_4-P that enhances the electron transfer, improves the active sites cavities, and maximizes the atomic utilization.

Chapter 7

Catalytic performance of the monometallic, bimetallic, and trimetallic catalysts; Fe/gC_3N_4-P, FeTi/gC_3N_4-P, and FeTiCu/gC_3N_4-P

7.1 Results and discussion

To further optimize the catalyst activity, Ti and Cu were introduced to prepare bimetallic and trimetallic catalysts, which can combine the catalytic properties of the three metals presenting higher catalytic performance than the monometallic catalysts.

7.1.1 Characterization

The FTIR analyses of the monometallic (Fe/gC_3N_4-P), bimetallic (FeTi/gC_3N_4-P), and trimetallic (FeTiCu/gC_3N_4-P) (Figure 7.1a) confirmed the successful preparation showing the band at 810 cm^{-1}, attributed to the s-triazine unit and the broad bands between 1100 and 1600 cm^{-1}, ascribed to the stretching mode of C-N in addition to the bands around 3200 cm^{-1}, ascribed to the N-H [45, 46]. However, The FTIR spectra did not show clear differences among the three catalysts. In addition, the XRD analysis of Fe/gC_3N_4-P, FeTi/gC_3N_4-P, and FeTiCu/gC_3N_4-P displayed the mother peak of carbon around 27.4 two theta, attributed to the [002] facet (Figure 7.1b) without detection of C [100] phase. The XRD did not show a difference among the three catalysts as well. The EDX analyses of the catalysts confirmed the presence of all metals in the catalysts (Figure 7.1c). Besides, the SEM images of Fe/gC_3N_4-P, FeTi/gC_3N_4-P, and FeTiCu/gC_3N_4-P confirmed again the hierarchical porous structure of the three catalysts as shown in Figures 7.1d-f, which confirms the successful preparation of the three catalysts by the polymerization method.

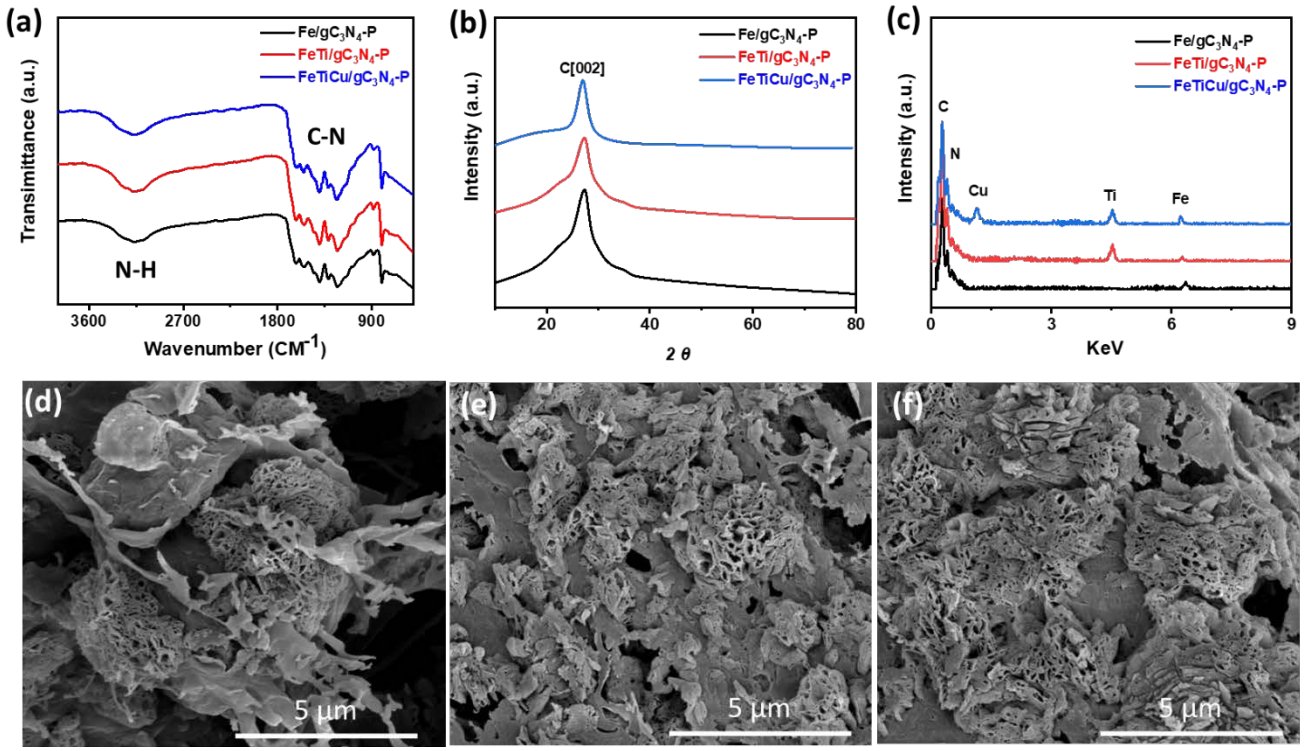

Figure 7.1. (a) FTIR, (b) XRD, and (c) EDX of Fe/gC_3N_4-P, FeTi/gC_3N_4-P, and FeTiCu/gC_3N_4-P, SEM images of (d) Fe/gC_3N_4-P, (e) FeTi/gC_3N_4-P, and (f) FeTiCu/gC_3N_4-P

The XPS full surface survey of Fe/gC_3N_4-P, FeTi/gC_3N_4-P, and FeTiCu/gC_3N_4-P confirmed the successful introducing of metals to each catalyst. The spectra of FeTi/gC_3N_4 showed the additional peak of Ti2p and the spectra of FeTiCu/gC_3N_4 showed the additional peaks of Ti2p and Cu2p (Figure 7.2a). The high-resolution spectra C1s of the catalysts showed the same range of the binding energy of C-C and C-N bonds without clear differences, which might be attributed to the low concentrations of the metals compared to C and N (Figures 7.2b-c). Also, the high-resolution spectra of N1s of the three catalysts showed similar range of binding energies confirming the existence of pyridinic, pyrrolic, and graphitic N species without clear differences among the three catalysts, which might be attributed to the low concentrations of the metal compared to C and N (Figures 7.2d-e). The high-resolution spectra of Fe2p of the three catalysts showed the two peaks of Fe; $Fe2p_{3/2}$

and $Fe2p_{1/2}$ at ~707 and ~723 eV respectively (Figures 20f-g) [67]. In addition, it is worthy noted that the peak fitting indicated that metallic Fe is the main phase. In addition, the high-resolution XPS spectra of the Ti2p regions of $FeTi/gC_3N_4$ and $FeTiCu/gC_3N_4$ showed two peaks around 455.6 and 461.1 eV, which are attributed to the $Ti2p_{3/2}$ and $Ti2p_{1/2}$, respectively (Figures 20h-i) matching with the reported results [68]. The peak fitting indicated that the main phase is the metallic Ti. Finally, the high-resolution XPS spectra of Cu of $FeTiCu/gC_3N_4$ showed the two regions of Cu2p around 933.1 and 951.3 eV, which representing $Cu2p_{3/2}$ and $Cu2p_{1/2}$, respectively [69]. In addition, the peak fitting of the $Cu2p_{3/2}$ and $Cu2p_{1/2}$ indicated that the main phase is metallic Cu (Figure 20j). The high-resolution spectra peaks of the three metals did not show clear difference among the three catalysts, which might be attributed to the low loadings of the metals.

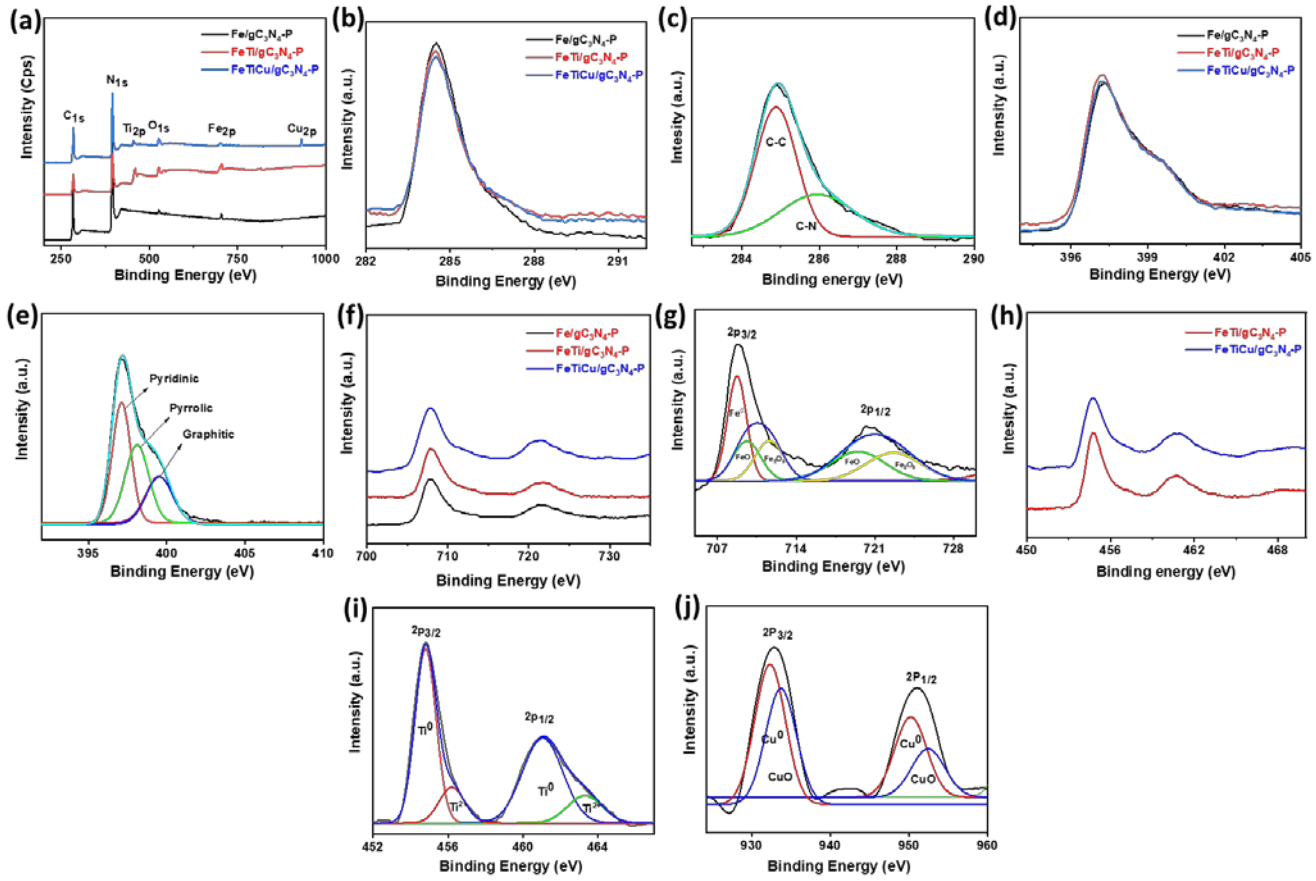

Figure 7.2. XPS full surface survey (a), High-resolution spectra of C1s and its interpretation (b-

c), High-resolution spectra of N1s and its interpretation (d-e), High-resolution spectra of Fe2p and its interpretation (f-g), High-resolution spectra of Ti2p and its interpretation (h-i), and the High-resolution spectra of Cu2p and its interpretation (j) of the prepared catalysts.

The TGA analyses of FeTi/gC_3N_4-P and FeTiCu/gC_3N_4-P showed close stable thermal behavior to the monometallic Fe/gC_3N_4-P as they stayed stable up to 600 °C. However, a slight faster decomposition occurred in FeTi/gC_3N_4-P and FeTiCu/gC_3N_4-P, representing the beginning of carbon oxidation, after 600 °C. The complete decomposition, representing the complete oxidation of carbon, occurred around 740 °C, which slightly earlier than Fe/gC_3N_4-P that stayed till 780 °C (Figure 7.3a). That slight lower thermal stability of FeTi/gC_3N_4-P and FeTiCu/gC_3N_4-P might be attributed to the less concentration of Fe, which has an effect on increasing the thermal stability [60, 61], as discussed earlier in chapter 5. In addition, Raman analysis of Fe/gC_3N_4-P, FeTi/gC_3N_4-P, and FeTiCu/gC_3N_4-P showed the two peaks corresponded to the D band and G band in the three catalysts in addition to the 2D band peak. However, the Fe/gC_3N_4-P presented a slight lower I_D/I_G ratio (0.93) than FeTi/gC_3N_4-P (0.94) and FeTiCu/gC_3N_4-P (0.95) (Figure 7.3b). That slight higher graphitization of Fe/gC_3N_4-P might be ascribed to the higher Fe content, which significantly increases the graphitization [62, 63], as previously discussed in chapter 5. The H_2-TPR analyses of Fe/gC_3N_4-P showed a broad peak of Hydrogen uptake with a maximum uptake around 300 °C and the FeTi/gC_3N_4-P presented a maximum hydrogen uptake about 250 °C, while FeTiCu/gC_3N_4-P offered the maximum hydrogen uptake at the lowest temperature around 190 °C. The H_2-TPR profiles of the three catalysts (Figure 7.3c) confirmed the reducibility trend, as addition of Ti and Cu to the monometallic Fe/gC_3N_4-P increases the reducibility [70-72]. CO-TPD profiles of the catalysts

showed similar behavior as FeTiCu/gC_3N_4-P offered the maximum peak of CO desorption around 150 °C only, while FeTi/gC_3N_4-P and Fe/gC_3N_4-P showed the maximum peak of CO desorption around 180 °C and 200 °C, respectively (Figure 7.3d). That improved sorption properties that enhance the tolerance transfer of intermediates might be attributed to the synergistic effect of Ti [73, 74] and Cu [75, 76] existed in FeTi/gC_3N_4-P and FeTiCu/gC_3N_4-P.

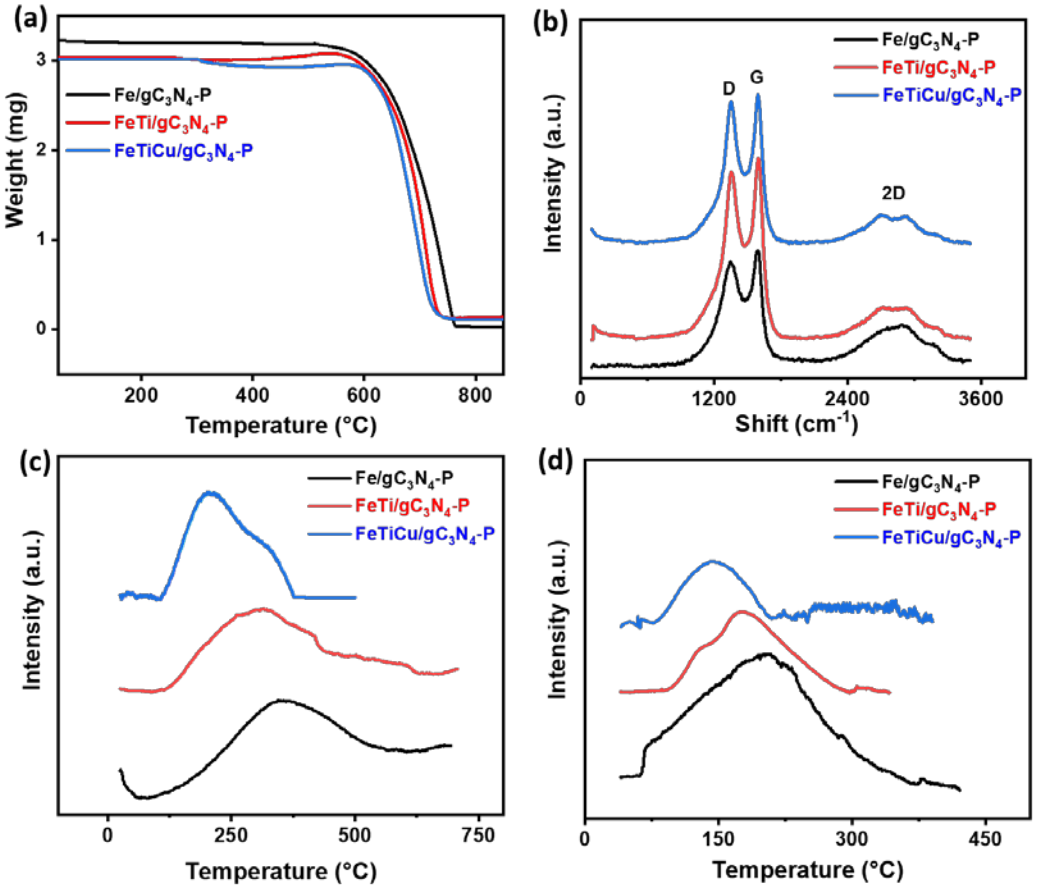

Figure 7.3. TGA (a), Raman (b), H_2-TPR (c), and CO-TPD of Fe/gC_3N_4-P, FeTi/gC_3N_4-P, and FeTiCu/gC_3N_4-P

7.1.2. Catalytic Tests

The catalytic tests were carried out at a temperature range of 24-300 °C and the catalysts Fe/gC_3N_4-P, FeTi/gC_3N_4-P, and FeTiCu/gC_3N_4-P achieved the complete CO conversion at T_{100} of 245 °C, 175 °C, and 147 °C, respectively (Figure 7.4a). FeTi/gC_3N_4-P showed higher catalytic activity than Fe/gC_3N_4-P, which is attributed to the enhanced reducibility and the synergistic effect with Ti [73, 74]. Moreover, FeTiCu/gC_3N_4-P offered the highest catalytic activity among the three catalysts, which is ascribed to the improved reducibility and the synergistic effect of Ti and Cu as well [75, 76]. In addition, the kinetic reactions at low CO conversions showed the same trend of catalytic activity as seen in Figure 7.4b. Besides, the spent catalyst FeTiCu/gC_3N_4-P was used for reducibility tests for three cycles and did not show any deactivation behavior (Figure 7.4c).

Furthermore, FeTiCu/gC_3N_4-P showed a stable behavior for more than 10 hours without any deactivation (Figure 7.4d). In a comparison with the commercial catalyst purchased from Sigma Aldrich (Pd/C-Comm), FeTiCu/gC_3N_4-P showed complete CO conversion at low (T_{100} = 147 °C), inferring higher catalytic activity than that of Pd/C-Comm (198 °C) (Figure 7.5a). In addition, FeTi/gC_3N_4-P showed also a higher catalytic activity than Pd/C-Comm with achieving the full CO conversion at T_{100} (175 °C). On the other hand, the monometallic Fe/gC_3N_4-P and Fe/gC_3N_4-M were inferior to the Pd/C-Comm as they achieved the complete CO conversion at T_{100} of 245 and 291 °C, respectively (Figure 7.5b).

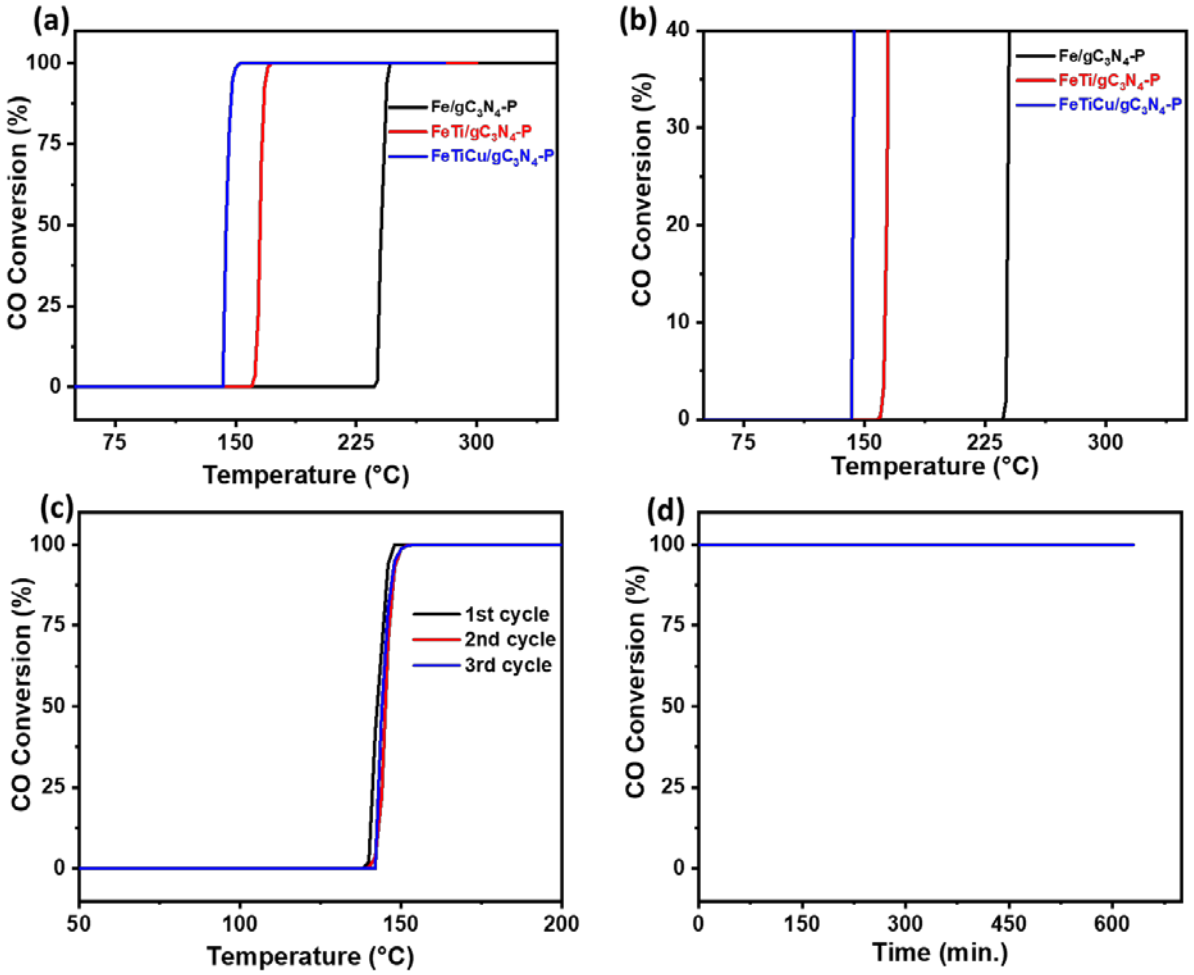

Figure 7.4. The catalytic activity (a) and the kinetic reactions (b) of Fe/gC_3N_4, $FeTi/gC_3N_4$, and $FeTiCu/gC_3N_4$. (c) Recycling tests and (d) stability test of $FeTiCu/gC_3N_4$.

Table 7.1. A comparison among the as-synthesized C_3N_x based catalysts

Catalyst	**C_3N_4 Preparation Method**	**T_{100} (°C)**
Fe/gC_3N_4-M	Mechanical Mixing	291
Fe/C_3N_5-M	Mechanical Mixing	322
Fe/C_3N_6-M	Mechanical Mixing	335
Fe/gC_3N_4-P	Polymerization method	245
$FeTi/gC_3N_4$-P	Polymerization method	175
$FeTiCu/gC_3N_4$-P	Polymerization method	147

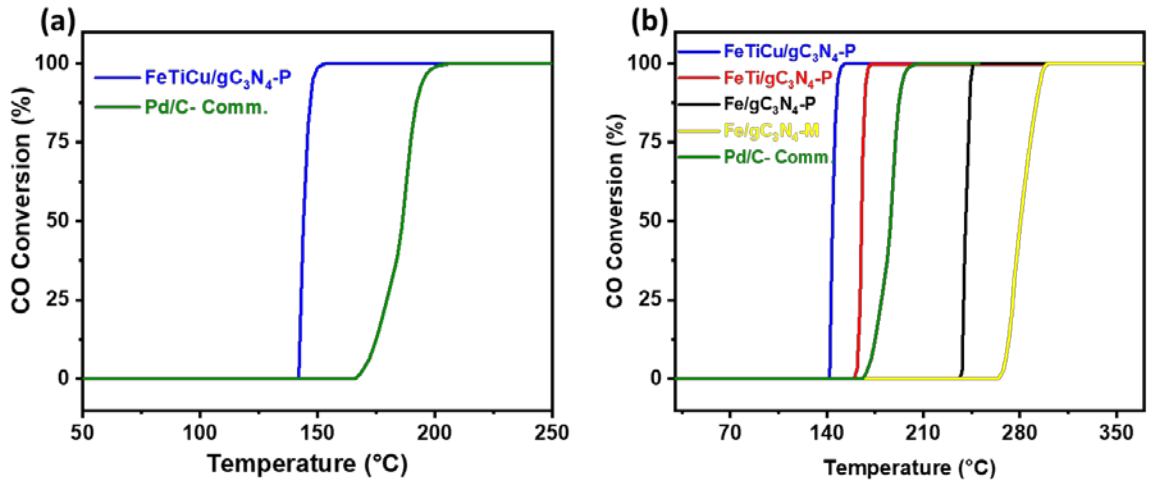

Figure 7.5 (a) A comparison between FeTiCu/gC_3N_4 and Pd/C-Comm. And (b) a comparison among the prepared gC_3N_4 based catalysts and Pd/C-Comm.

7.2. Conclusions

FTIR, XPS, and XRD analyses confirmed the successful preparation of the monometallic Fe/gC_3N_4-P, bimetallic FeTi/gC_3N_4-P, and trimetallic FeTiCu/gC_3N_4-P. In addition, the XPS and EDX analyses confirmed the perfect addition of Fe, Ti, and Cu to the three catalysts. The SEM images confirmed the existence of the hierarchical porous structures in Fe/gC_3N_4-P, FeTi/gC_3N_4-P, and FeTiCu/gC_3N_4-P. Besides, Raman analysis showed a slightly higher graphitization degree for Fe/gC_3N_4-P, which is attributed to the higher Fe content. FeTiCu/gC_3N_4-P (T_{100}147) and FeTi/gC_3N_4-P (T_{100}175) showed higher catalytic activity than Fe/gC_3N_4-P (T_{100}245), which is attributed to the enhanced reducibility and synergistic effect caused by Ti and Cu. Moreover, FeTi/gC_3N_4-P and FeTiCu/gC_3N_4-P presented higher catalytic activity than the commercial catalyst Pd/C-Comm. (T_{100}198), while Fe/gC_3N_4-P was inferior to it. FeTiCu/gC_3N_4-P presented the highest catalytic activity among all tested catalysts (Table 7) in addition to a stable behavior for more than ten hours.

Chapter 8

Conclusions and recommendations

8.1. Conclusions

FTIR, XPS, and EDX analyses confirmed the successful formation of the different phases of carbon nitride (gC_3N_4, C_3N_5, and C_3N_6) in addition to the successful preparation of Fe supported on them (Fe/gC_3N_4, Fe/C_3N_5, and Fe/C_3N_6). Moreover, the XRD analyses showed that the gC_3N_4 phase is more crystalized than C_3N_5 and C_3N_6. Besides, the TGA Showed a significant difference among the three phases as the gC_3N_4 was more thermally stable than C_3N_5 and C_3N_6. In addition, XRD analyses indicated that Fe addition increased the crystallinity of gC_3N_4, C_3N_5, and C_3N_6 and confirmed that Fe/gC_3N_4 is more crystalized than Fe/C_3N_5 and Fe/C_3N_6. Moreover, the TGA showed an increase in the thermal stability of gC_3N_4, C_3N_5, and C_3N_6 after the addition of Fe. Furthermore, the Raman analysis showed clearly that Fe addition significantly increased the graphitization of the three catalysts and mainly the Fe/gC_3N_4-M, which showed higher graphitization degree than Fe/C_3N_5-M and Fe/C_3N_6-M. Accordingly, Fe/gC_3N_4 achieved high catalytic activity, presenting complete CO conversion at 291 °C superior to Fe/C_3N_5-M (T_{100}= 322 °C) and Fe/C_3N_6-M (T_{100}= 335 °C).

Preparation of Fe/gC_3N_4-P by the Polymerization method was also confirmed by the FTIR, EDX, and XPS analyses. In addition, the SEM images confirmed the formation of the hierarchical porous structures of Fe/gC_3N_4-P clearly, and the BET surface area of Fe/gC_3N_4-P (219 m2/g) was far higher than Fe/gC_3N_4-M (77 m2/g), which is attributed to the unique preparation technique. Accordingly, the catalytic activity of Fe/gC_3N_4-P was higher than that of Fe/gC_3N_4-M as Fe/gC_3N_4-P achieved the complete CO conversion at 246 °C, while Fe/gC_3N_4-M achieved it at 291 °C. Furthermore, the

monometallic catalyst Fe/gC_3N_4-P was optimized by the addition of Ti and Cu to obtain bimetallic FeTi/gC_3N_4-P (T_{100}= 175 ^oC) and trimetallic FeTiCu/gC_3N_4-P (T_{100}= 147 ^oC), which showed higher catalytic activity than the monometallic Fe/gC_3N_4-P (T_{100}= 245 ^oC), which is attributed to the enhanced reducibility and synergistic effect caused by Ti and Cu.

Moreover, FeTi/gC_3N_4-P (T_{100}= 175 ^oC) and FeTiCu/gC_3N_4-P (T_{100}= 147 ^oC) showed higher catalytic activity than the commercial catalyst Pd/C-Comm. (T_{100}= 198 ^oC), while Fe/gC_3N_4-P (T_{100}= 245 ^oC) was inferior to it. FeTiCu/gC_3N_4-P presented the highest catalytic activity among all tested catalysts and showed a stable behavior for more than ten hours in addition to three cycles of reproducibility. In a comparison between the developed catalyst FeTiCu/gC_3N_4-P and other reported catalysts, it is clear that we could prepare and optimize a highly active catalyst made from available transition metals supported on cheap carbon material. FeTiCu/gC_3N_4-P (T_{100}= 147 ^oC) showed higher catalytic activity than all reported transition metals supported gC_3N_4 catalysts (Table 8.1) except Co_3O_4/g-C_3N_4 (T_{100}= 120 ^oC)[31]. Moreover, FeTiCu/gC_3N_4-P was also more active than all reported noble metals supported gC_3N_4 catalysts except Pt/CN-600 (T_{100}= 85 ^oC), Pt/CN-650 (T_{100}= 100 ^oC), and Pt/CN-700 (T_{100}= 130 ^oC)[22] and it was very close to Au/Pd/gC_3N_4-NFs(T_{100}= 144 ^oC)[5]. Furthermore, FeTiCu/gC_3N_4-P was more active than other catalysts supported on different materials, such as silica[29], alumina[77], and titania[22], as shown in Table 8.1.

Table 8.1. A comparison among different catalysts to evaluate our optimized catalysts

Catalyst	**gC_3N_4 Preparation Method**	**T_{100} (°C)**	**Ref.**
Transition metals supported gC_3N_4 catalysts			
Cu-P-gC_3N_4	Polymerization method	184	[42]

$Cu_2O/g\text{-}C_3N_4$	Pyrolysis	200	[30]
$Co_3O_4/g\text{-}C_3N_4$	Pyrolysis	120	[31]
Co_3O_4/mpg-CN	Hydrothermal Synthesis	160	[32]
Co/CN/SBA-16	Hydrothermal Synthesis	175	[33]
Cu/gC_3N_4NTs	Polymerization method	250	[2]
Noble metals supported gC_3N_4 catalysts			
Pt-CNx/SBA(15)$_{500}$	Pyrolysis	160	[29]
Pt-CN600	Pyrolysis	130	[22]
Pt-CN650		100	[22]
Pt-CN700		85	[22]
PdCu/CNNWs	Polymerization method	149	[34]
Au-Pd/gC_3N_4-NTs	Polymerization method	165	[35]
Pd/gC_3N_4-NTs	Polymerization method	210	[2]
Pd/Cu/gC_3N_4-NTs		154	[2]
Pd/gC_3N_4-NFs	Polymerization method	191	[5]
Au/Pd/gC_3N_4-NFs		144	[5]
Catalysts on different supports other than gC_3N_4			
Fe/CeO_2	coprecipitation	300	[21]
$\alpha\text{-}Fe_2O_3$	Hydrothermal Synthesis	255	[64]
$\alpha\text{-}Fe_2O_3$- flowerlike	Solvothermal Synthesis	260	[78]
$\alpha\text{-}Fe_2O_3$- quasicubic		230	[78]
$\alpha\text{-}Fe_2O_3$	Hydrothermal Synthesis	300	[79]
Pt/SBA-15	Pyrolysis	250	[29]
Pt/TiO_2	Pyrolysis	150	[22]
Pd-E-graphene	Microwave-assisted	190	[80]

Pd-D-graphene	synthesis	210	[80]
CuO/TiO_2	Sol-gel	245	[81]
CuO/TiO_2		327	[81]
$Au-Cu/SiO_2$	Impregnation	300	[82]
$AuPd/TiO_2$	Incipient wetness	190	[83]
CuO/CeO_2	Pyrolysis	150	[84]
Pd/CeO_2	Impregnation	150	[85]
Pd/UiO-66	Solvothermal Synthesis	165	[86]
$Pd-Co/Al_2O_3$	Solvothermal Synthesis	180	[77]
$Pd-Co/Al_2O_3$		110	[77]
Pt/CeO[87]	hydrothermal Synthesis	98	[87]
$FeTiCu/gC_3N_4-P$	Polymerization method	147	This
$FeTi/gC_3N_4-P$		175	work
Fe/gC_3N_4-P		245	

8.2. Recommendations

Synthesis techniques of C_3N_x loaded with metals require to be developed to improve the catalytic properties and enhance the catalytic performance. Porous structures are commonly synthesized by template-based methods. Thus, template-free preparation should be optimized to save the additional consumed chemicals[88]. In addition, the icing-assisted photocatalytic technique is a promising path for the preparation of bimetallic carbon-based catalysts[89]. In addition, Using the single atom catalysts and the high entropy metal alloys may enhance the catalytic performance of C_3N_x-based catalysts[90]. Moreover, impregnation of C_3N_x with new materials, such as MXenes[91], and graphene[92], may also improve the CO oxidation. Furthermore, the earth-abundant non-metal traces such as S, and P may promote the catalysts of the CO oxidation due to their excellent electronic and basic advantages[93]. The hierarchical multidimensional structures of C_3N_x, such as nanodendrites, and nanoflowers are rarely investigated in the catalytic CO oxidation. However, those structures can strongly improve the catalytic performance, owing to their unique surface area and abundant active sites, which can maximize atomic utilization and improve electron transfer [93-96]. Furthermore, microwave-assisted heating is a promising technique for replacing traditional heating, which can offer less economical cost and less time consumption[97].

References

[1] Eid K, Sliem MH, Abdullah AM. Unraveling template-free fabrication of carbon nitride nanorods codoped with Pt and Pd for efficient electrochemical and photoelectrochemical carbon monoxide oxidation at room temperature. Nanoscale. 2019;11:11755-64.

[2] Eid K, Sliem MH, Jlassi K, Eldesoky AS, Abdo GG, Al-Qaradawi SY, et al. Precise fabrication of porous one-dimensional gC3N4 nanotubes doped with Pd and Cu atoms for efficient CO oxidation and CO2 reduction. Inorganic Chemistry Communications. 2019;107:107460.

[3] Eid K, Abdullah AM. Data on the catalytic CO oxidation and CO2 reduction durability on gC3N4 nanotubes Co-doped atomically with Pd and Cu. Data in brief. 2019;26:104495.

[4] Eid K, Sliem MH, Eldesoky AS, Abdullah AM. Data on structural and composition-related merits of gC3N4 nanofibres doped and undoped with Au/Pd at the atomic level for efficient catalytic CO oxidation. Data in brief. 2019;27:104734.

[5] Eid K, Sliem MH, Eldesoky AS, Al-Kandari H, Abdullah AM. Rational synthesis of one-dimensional carbon nitride-based nanofibers atomically doped with Au/Pd for efficient carbon monoxide oxidation. International Journal of Hydrogen Energy. 2019;44:17943-53.

[6] Yang F, Graciani J, Evans J, Liu P, Hrbek J, Sanz JF, et al. CO Oxidation on inverse CeO x/Cu (111) catalysts: High catalytic activity and ceria-promoted dissociation of O2. Journal of the American Chemical Society. 2011;133:3444-51.

[7] No HC, Kadak A. Depressurization Accident Analysis of MPBR by PBR_SIM with Chemical Reaction Model. Proceedings of the Korean Nuclear Society Conference: Korean Nuclear Society; 2002. p. 186-.

[8] Stewart RD. The effect of carbon monoxide on humans. Annual review of pharmacology. 1975;15:409-23.

[9] Badr O, Probert S. Carbon□ monoxide concentration in the Earth's atmosphere. Applied Energy. 1994;49:99-143.

[10] Carnis J, Kshirsagar AR, Wu L, Dupraz M, Labat S, Texier M, et al. Twin boundary migration in an individual platinum nanocrystal during catalytic CO oxidation. Nature communications. 2021;12:1-10.

[11] Liu L, Corma A. Metal catalysts for heterogeneous catalysis: from single atoms to nanoclusters and nanoparticles. Chemical reviews. 2018;118:4981-5079.

[12] Xu H, Xu C-Q, Cheng D, Li J. Identification of activity trends for CO oxidation on supported transition-metal single-atom catalysts. Catalysis Science & Technology. 2017;7:5860-

71.
[13] Elias JS, Stoerzinger KA, Hong WT, Risch M, Giordano L, Mansour AN, et al. In situ spectroscopy and mechanistic insights into CO oxidation on transition-metal-substituted ceria nanoparticles. ACS Catalysis. 2017;7:6843-57.
[14] Davó-Quiñonero A, López-Rodríguez S, Bailón-García E, Lozano-Castello D, Bueno-López A. Mineral Manganese Oxides as Oxidation Catalysts: Capabilities in the CO-PROX Reaction. ACS Sustainable Chemistry & Engineering. 2021;9:6329-36.
[15] Burmeister D, Trunk MG, Bojdys MJ. Development of metal-free layered semiconductors for 2D organic field-effect transistors. Chemical Society Reviews. 2021.
[16] Zhou L, Zhang Z, Li M, Wang Q, Gao J, Li K, et al. Graphitic carbon nitride (gC 3 N 4) as a sustainable heterogeneous photocatalyst for metal free and oxygen-tolerant photo-atom transfer radical polymerization (photo-ATRP). Green Chemistry. 2021;23:9617-24.
[17] Yang X, Ma J, Sun S, Liu Z, Sun R. K/O co-doping and introduction of cyano groups in polymeric carbon nitride towards efficient simultaneous solar photocatalytic water splitting and biorefinery. Green Chemistry. 2022.
[18] Catherine HN, Liu Z-T, Lin C-Y, Chung P-W, Tsunekawa S, Lin SD, et al. Understanding the intermediates and carbon dioxide adsorption of potassium chloride-incorporated graphitic carbon nitride with tailoring melamine and urea as precursors. Journal of Colloid and Interface Science. 2023;633:598-607.
[19] Hu C, Lin Y-H, Yoshida M, Ashimura S. Influence of phosphorus doping on triazole-based g-C3N5 nanosheets for enhanced photoelectrochemical and photocatalytic performance. ACS Applied Materials & Interfaces. 2021;13:24907-15.
[20] Talapaneni SN, Mane GP, Park D-H, Lakhi KS, Ramadass K, Joseph S, et al. Diaminotetrazine based mesoporous C 3 N 6 with a well-ordered 3D cubic structure and its excellent photocatalytic performance for hydrogen evolution. Journal of Materials Chemistry A. 2017;5:18183-92.
[21] Sudarsanam P, Mallesham B, Durgasri DN, Reddy BM. Physicochemical characterization and catalytic CO oxidation performance of nanocrystalline Ce–Fe mixed oxides. Rsc Advances. 2014;4:11322-30.
[22] Wu P, Wu Z, Mullins DR, Yang S-Z, Han X, Zhang Y, et al. Promoting Pt catalysis for CO oxidation via the Mott–Schottky effect. Nanoscale. 2019;11:18568-74.
[23] Dey S, Dhal GC. A review of synthesis, structure and applications in hopcalite catalysts for carbon monoxide oxidation. Aerosol Science and Engineering. 2019:1-35.
[24] Dey S, Dhal GC, Mohan D, Prasad R. Advances in transition metal oxide catalysts for

carbon monoxide oxidation: a review. Advanced Composites and Hybrid Materials. 2019:1-31.
[25] Peng C, Han L, Huang J, Wang S, Zhang X, Chen H. Comprehensive investigation on robust photocatalytic hydrogen production over C3N5. Chinese Journal of Catalysis. 2022;43:410-20.
[26] Li Q, Song S, Mo Z, Zhang L, Qian Y, Ge C. Hollow carbon nanospheres@ graphitic C3N5 heterostructures for enhanced oxygen electroreduction. Applied Surface Science. 2022;579:152006.
[27] Sathish C, Premkumar S, Chu X, Yu X, Breese MB, Al-Abri M, et al. Microporous carbon nitride (C3N5. 4) with tetrazine based molecular structure for efficient adsorption of CO2 and water. Angewandte Chemie International Edition. 2021;60:21242-9.
[28] Binder AJ, Qiao Z-A, Veith GM, Dai S. Deposition–precipitation and stabilization of a silica-supported Au catalyst by surface modification with carbon nitride. Catalysis letters. 2013;143:1339-45.
[29] Xiao P, Zhao Y, Wang T, Zhan Y, Wang H, Li J, et al. Polymeric carbon nitride/mesoporous silica composites as catalyst support for Au and Pt nanoparticles. Chemistry–A European Journal. 2014;20:2872-8.
[30] Shi Y, Hu X, Zhao J, Zhou X, Zhu B, Zhang S, et al. CO oxidation over Cu 2 O deposited on 2D continuous lamellar gC 3 N 4. New Journal of Chemistry. 2015;39:6642-8.
[31] Wang Y, Huang J, Cao J, Li G, Zhang Z. Cobalt oxide decorated flower-like g-C3N4 hybrid nanomaterials for carbon monoxide oxidation. Surface Review and Letters. 2017;24:1750058.
[32] Yang H, Lv K, Zhu J, Li Q, Tang D, Ho W, et al. Effect of mesoporous g-C3N4 substrate on catalytic oxidation of CO over Co3O4. Applied Surface Science. 2017;401:333-40.
[33] Yang H, Yang W, Lv K, Zhu J, Xia Y, Tang D, et al. Effect of the structure of CN/Silica composite support on the catalytic performances of Co3O4 for CO oxidation. Microporous and Mesoporous Materials. 2018;255:36-43.
[34] Eid K, Ahmad YH, Mohamed AT, Elsafy AG, Al-Qaradawi SY. Versatile synthesis of Pd and Cu Co-doped porous carbon nitride nanowires for catalytic CO oxidation reaction. Catalysts. 2018;8:411.
[35] Eid K, Sliem MH, Al-Kandari H, Sharaf MA, Abdullah AM. Rational synthesis of porous graphitic-like carbon nitride nanotubes codoped with Au and Pd as an efficient catalyst for carbon monoxide oxidation. Langmuir. 2019;35:3421-31.
[36] Dey S, Dhal GC. Materials progress in the control of CO and CO2 emission at ambient conditions: An overview. Materials Science for Energy Technologies. 2019;2:607-23.
[37] Petrov L, Alhamed Y, Al-Zahrani A, Daous M. Role of chemical kinetics in the

heterogeneous catalysis studies. Chinese Journal of Catalysis. 2011;32:1085-112.
[38] Saqlain MA, Hussain A, Siddiq M, Leitão AA. A DFT+ U study of the Mars Van Krevelen mechanism of CO oxidation on Au/TiO2 catalysts. Applied Catalysis A: General. 2016;519:27-33.
[39] Salomons S, Votsmeier M, Hayes R, Drochner A, Vogel H, Gieshof J. CO and H2 oxidation on a platinum monolith diesel oxidation catalyst. Catalysis Today. 2006;117:491-7.
[40] Li F, Zhao J, Chen Z. Fe-anchored graphene oxide: a low-cost and easily accessible catalyst for low-temperature CO oxidation. The Journal of Physical Chemistry C. 2012;116:2507-14.
[41] Lyu P, He J, Nachtigall P. Theoretical investigation of CO catalytic oxidation by a Fe–PtSe 2 monolayer. RSC advances. 2017;7:19630-8.
[42] Eid K, Sliem MH, Al-Ejji M, Abdullah AM, Harfouche M, Varma RS. Hierarchical Porous Carbon Nitride-Crumpled Nanosheet-Embedded Copper Single Atoms: An Efficient Catalyst for Carbon Monoxide Oxidation. ACS Applied Materials & Interfaces. 2022;14:40749-60.
[43] To D-T, Juan JC, Tsai M-H, Wang C-H, Pao C-W, Chen C-L, et al. Conversion of CO2 to Light Hydrocarbons by Using FeCx Catalysts Derived from Iron Nitrate Co-pyrolyzing with Melamine, Bulk g-C3N4, or Defective g-C3N4. Catalysis Surveys from Asia. 2023:1-10.
[44] Sathish C, Premkumar S, Chu X, Yu X, Breese MB, Al-Abri M, et al. Microporous carbon nitride (C3N5. 4) with tetrazine based molecular structure for efficient adsorption of CO2 and water. Angewandte Chemie. 2021;133:21412-9.
[45] Talapaneni SN, Mane GP, Mano A, Anand C, Dhawale DS, Mori T, et al. Synthesis of nitrogen-rich mesoporous carbon nitride with tunable pores, band gaps and nitrogen content from a single aminoguanidine precursor. ChemSusChem. 2012;5:700-8.
[46] Levchik SV, Ivashkevich O, Balabanovich A, Lesnikovich A, Gaponik P, Costa L. Thermal decomposition of aminotetrazoles: Part 1. 5-Aminotetrazole. Thermochimica acta. 1992;207:115-30.
[47] Kim IY, Kim S, Premkumar S, Yang JH, Umapathy S, Vinu A. Thermodynamically stable mesoporous C3N7 and C3N6 with ordered structure and their excellent performance for oxygen reduction reaction. Small. 2020;16:1903572.
[48] Zhang L, Zhang J, Xia Y, Xun M, Chen H, Liu X, et al. Metal-free carbon quantum dots implant graphitic carbon nitride: Enhanced photocatalytic dye wastewater purification with simultaneous hydrogen production. International Journal of Molecular Sciences. 2020;21:1052.
[49] Ge L, Han C. Synthesis of MWNTs/g-C3N4 composite photocatalysts with efficient visible light photocatalytic hydrogen evolution activity. Applied Catalysis B: Environmental. 2012;117:268-74.

[50] Li Y, Sun Y, Li H, Sun M, Shen J, Wang S. High nitrogen-oxygen dual-doped three-dimensional hierarchical porous carbon network derived from Eriocheir sinensis for advanced supercapacitors. Energy. 2023:126942.
[51] Maldonado S, Morin S, Stevenson KJ. Structure, composition, and chemical reactivity of carbon nanotubes by selective nitrogen doping. Carbon. 2006;44:1429-37.
[52] Morant C, Andrey J, Prieto P, Mendiola D, Sanz J, Elizalde E. XPS characterization of nitrogen-doped carbon nanotubes. physica status solidi (a). 2006;203:1069-75.
[53] Azuara-Tuexi G, Muñoz-Sandoval E, Guirado-López R. N 1s core-level binding energies in nitrogen-doped carbon nanotubes: a combined experimental and theoretical study. Physical Chemistry Chemical Physics. 2023;25:3718-36.
[54] Dai H, Gao X, Liu E, Yang Y, Hou W, Kang L, et al. Synthesis and characterization of graphitic carbon nitride sub-microspheres using microwave method under mild condition. Diamond and Related Materials. 2013;38:109-17.
[55] Li Y, Yang M, Xing Y, Liu X, Yang Y, Wang X, et al. Preparation of Carbon-Rich g-C3N4 Nanosheets with Enhanced Visible Light Utilization for Efficient Photocatalytic Hydrogen Production. Small. 2017;13:1701552.
[56] Sole C, Drewett NE, Hardwick LJ. In situ Raman study of lithium-ion intercalation into microcrystalline graphite. Faraday Discussions. 2014;172:223-37.
[57] Sadiq M, Aman R, Hussain S, Zia MA, Rahman NU, Saeed M. Green and efficient oxidation of octanol by iron oxide nanoparticles supported on activated carbon. Modern Research in Catalysis. 2015;4:28.
[58] Almutawah ZS, Watthage SC, Song Z, Ahangharnejhad RH, Subedi KK, Shrestha N, et al. Enhanced grain size and crystallinity in CH 3 NH 3 PbI 3 perovskite films by metal additives to the single-step solution fabrication process. MRS Advances. 2018;3:3237-42.
[59] Liao F, Lo TWB, Sexton D, Qu J, Wu C-T, Tsang SCE. PdFe nanoparticles as selective catalysts for C–C cleavage in hydrogenolysis of vicinal diol units in biomass-derived chemicals. Catalysis Science & Technology. 2015;5:887-96.
[60] Zhang J, Li L, Chen G, Wee P. Influence of iron content on thermal stability of magnetic polyurethane foams. Polymer degradation and stability. 2009;94:246-52.
[61] Bingham P, Hand R, Forder S. Doping of iron phosphate glasses with Al2O3, SiO2 or B2O3 for improved thermal stability. Materials Research Bulletin. 2006;41:1622-30.
[62] Grudzinski IP, Bystrzejewski M, Bogorodzki P, Cieszanowski A, Szeszkowski W, Poplawska M, et al. Comprehensive magnetic resonance characteristics of carbon-encapsulated iron nanoparticles: a new frontier for the core-shell–type contrast agents. Journal of Nanoparticle

Research. 2020;22:1-17.
[63] Gomez-Martin A, Schnepp Z, Ramirez-Rico J. Structural evolution in iron-catalyzed graphitization of hard carbons. Chemistry of Materials. 2021;33:3087-97.
[64] Cui L, Zhao D, Yang Y, Wang Y, Zhang X. Synthesis of highly efficient α-Fe2O3 catalysts for CO oxidation derived from MIL-100 (Fe). Journal of Solid State Chemistry. 2017;247:168-72.
[65] Nurdin I, Johan MR, Yaacob II, Ang BC. Effect of nitric acid concentrations on synthesis and stability of maghemite nanoparticles suspension. The Scientific World Journal. 2014;2014.
[66] Prajapati AK, Mondal MK. Green synthesis of Fe3O4-onion peel biochar nanocomposites for adsorption of Cr (VI), methylene blue and congo red dye from aqueous solutions. Journal of Molecular Liquids. 2022;349:118161.
[67] Isimjan TT, El Ruby A, Rohani S, Ray AK. The fabrication of highly ordered and visible-light-responsive Fe–C–N-codoped TiO2 nanotubes. Nanotechnology. 2009;21:055706.
[68] Zhang P, Li Y, Zhang Y, Hou R, Zhang X, Xue C, et al. Photogenerated electron transfer process in heterojunctions: in situ irradiation XPS. Small Methods. 2020;4:2000214.
[69] Sun B, Li H, Li X, Liu X, Zhang C, Xu H, et al. Degradation of organic dyes over fenton-like Cu2O–Cu/C catalysts. Industrial & Engineering Chemistry Research. 2018;57:14011-21.
[70] Hwang K-R, Ihm S-K, Park S-C, Park J-S. Pt/ZrO2 catalyst for a single-stage water-gas shift reaction: Ti addition effect. International Journal of Hydrogen Energy. 2013;38:6044-51.
[71] Martínez N, García R, Fierro J, Wheeler C, Austin R, Gallagher J, et al. Effect of Cu addition as a promoter on Re/SiO2 catalysts in the hydrodeoxygenation of 2-methoxyphenol as a model bio oil compound. Fuel. 2016;186:112-21.
[72] Smith ML, Campos A, Spivey JJ. Reduction processes in Cu/SiO2, Co/SiO2, and CuCo/SiO2 catalysts. Catalysis Today. 2012;182:60-6.
[73] Park S, Thuy DT, Sarwar S, Van Tran H, Lee SI, Park HS, et al. Synergistic effects of Ti-doping induced porous networks on electrochromic performance of WO 3 films. Journal of Materials Chemistry C. 2020;8:17245-53.
[74] Chen D, He F, Han B, Wu Q, Tong Y, Zhao Y, et al. Synergistic effect of Ti and Al on L12-phase design in CoCrFeNi-based high entropy alloys. Intermetallics. 2019;110:106476.
[75] Yu Y, Dong Xa, Chen P, Geng Q, Wang H, Li J, et al. Synergistic effect of Cu single atoms and Au–Cu alloy nanoparticles on TiO2 for efficient CO2 photoreduction. ACS nano. 2021;15:14453-64.
[76] Khalid A, Ahmad P, Alharthi AI, Muhammad S, Khandaker MU, Faruque MRI, et al. Synergistic effects of Cu-doped ZnO nanoantibiotic against Gram-positive bacterial strains.

PLoS One. 2021;16:e0251082.
[77] Wu CH, Liu C, Su D, Xin HL, Fang H-T, Eren B, et al. Bimetallic synergy in cobalt–palladium nanocatalysts for CO oxidation. Nature Catalysis. 2019;2:78-85.
[78] Zheng Y, Cheng Y, Wang Y, Bao F, Zhou L, Wei X, et al. Quasicubic α-Fe2O3 nanoparticles with excellent catalytic performance. The Journal of Physical Chemistry B. 2006;110:3093-7.
[79] Liu X, Liu J, Chang Z, Sun X, Li Y. Crystal plane effect of Fe2O3 with various morphologies on CO catalytic oxidation. Catalysis Communications. 2011;12:530-4.
[80] Kumar R, Oh J-H, Kim H-J, Jung J-H, Jung C-H, Hong WG, et al. Nanohole-structured and palladium-embedded 3D porous graphene for ultrahigh hydrogen storage and CO oxidation multifunctionalities. ACS nano. 2015;9:7343-51.
[81] Fang Y, Chi X, Li L, Yang J, Liu S, Lu X, et al. Elucidating the Nature of the Cu (I) Active Site in CuO/TiO2 for Excellent Low-Temperature CO Oxidation. ACS applied materials & interfaces. 2020;12:7091-101.
[82] Destro P, Marras S, Manna L, Colombo M, Zanchet D. AuCu alloy nanoparticles supported on SiO2: Impact of redox pretreatments in the catalyst performance in CO oxidation. Catalysis Today. 2017;282:105-10.
[83] Teixeira-Neto A, Gonçalves R, Rodella C, Rossi L, Teixeira-Neto E. Surface composition and structural changes on titanium oxide-supported AuPd nanoparticles during CO oxidation. Catalysis Science & Technology. 2017;7:1679-89.
[84] Zheng X, Zhang X, Wang X, Wang S, Wu S. Preparation and characterization of CuO/CeO2 catalysts and their applications in low-temperature CO oxidation. Applied Catalysis A: General. 2005;295:142-9.
[85] Muravev V, Spezzati G, Su Y-Q, Parastaev A, Chiang F-K, Longo A, et al. Interface dynamics of Pd–CeO2 single-atom catalysts during CO oxidation. Nature Catalysis. 2021;4:469-78.
[86] Bi F, Zhang X, Du Q, Yue K, Wang R, Li F, et al. Influence of pretreatment conditions on low-temperature CO oxidation over Pd supported UiO-66 catalysts. Molecular Catalysis. 2021;509:111633.
[87] Wang C, Gu X-K, Yan H, Lin Y, Li J, Liu D, et al. Water-mediated Mars–van Krevelen mechanism for CO oxidation on ceria-supported single-atom Pt1 catalyst. Acs Catalysis. 2017;7:887-91.
[88] Cheung O, Zhang P, Frykstrand S, Zheng H, Yang T, Sommariva M, et al. Nanostructure and pore size control of template-free synthesised mesoporous magnesium carbonate. RSC

advances. 2016;6:74241-9.
[89] Zhou P, Hou X, Chao Y, Yang W, Zhang W, Mu Z, et al. Synergetic interaction between neighboring platinum and ruthenium monomers boosts CO oxidation. Chemical science. 2019;10:5898-905.
[90] Ipadeola AK, Lebechi AK, Gaolatlhe L, Haruna AB, Chitt M, Eid K, et al. Porous high-entropy alloys as efficient electrocatalysts for water-splitting reactions. Electrochemistry Communications. 2022;136:107207.
[91] Salah B, Eid K, Abdelgwad AM, Ibrahim Y, Abdullah AM, Hassan MK, et al. Titanium Carbide (Ti3C2Tx) MXene Ornamented with Palladium Nanoparticles for Electrochemical CO Oxidation. Electroanalysis. 2021.
[92] Abdu HI, Eid K, Abdullah AM, Sliem MH, Elzatahry A, Lu X. Dry ice-mediated rational synthesis of edge-carboxylated crumpled graphene nanosheets for selective and prompt hydrolysis of cellulose and eucalyptus lignocellulose under ambient reaction conditions. Green Chemistry. 2020;22:5437-46.
[93] Lu Q, Eid K, Li W, Abdullah AM, Xu G, Varma RS. Engineering graphitic carbon nitride (gC 3 N 4) for catalytic reduction of CO 2 to fuels and chemicals: strategy and mechanism. Green Chemistry. 2021;23:5394-428.
[94] Verma SK, Verma R, Girish YR, Xue F, Yan L, Verma S, et al. Heterogeneous graphitic carbon nitrides in visible-light-initiated organic transformations. Green Chemistry. 2022;24:438-79.
[95] Li Y-Y, Zhou B-X, Zhang H-W, Huang T, Wang Y-M, Huang W-Q, et al. A host–guest self-assembly strategy to enhance π-electron densities in ultrathin porous carbon nitride nanocages toward highly efficient hydrogen evolution. Chemical Engineering Journal. 2022;430:132880.
[96] Wu M, Gong Y, Nie T, Zhang J, Wang R, Wang H, et al. Template-free synthesis of nanocage-like gC 3 N 4 with high surface area and nitrogen defects for enhanced photocatalytic H 2 activity. Journal of Materials Chemistry A. 2019;7:5324-32.
[97] Fan S, Zhang Y, Cui L, Xiong Q, Maqsood T. Conversion of Polystyrene Plastic into Aviation Fuel through Microwave-Assisted Pyrolysis as Affected by Iron-Based Microwave Absorbents. ACS Sustainable Chemistry & Engineering. 2023.

Appendix

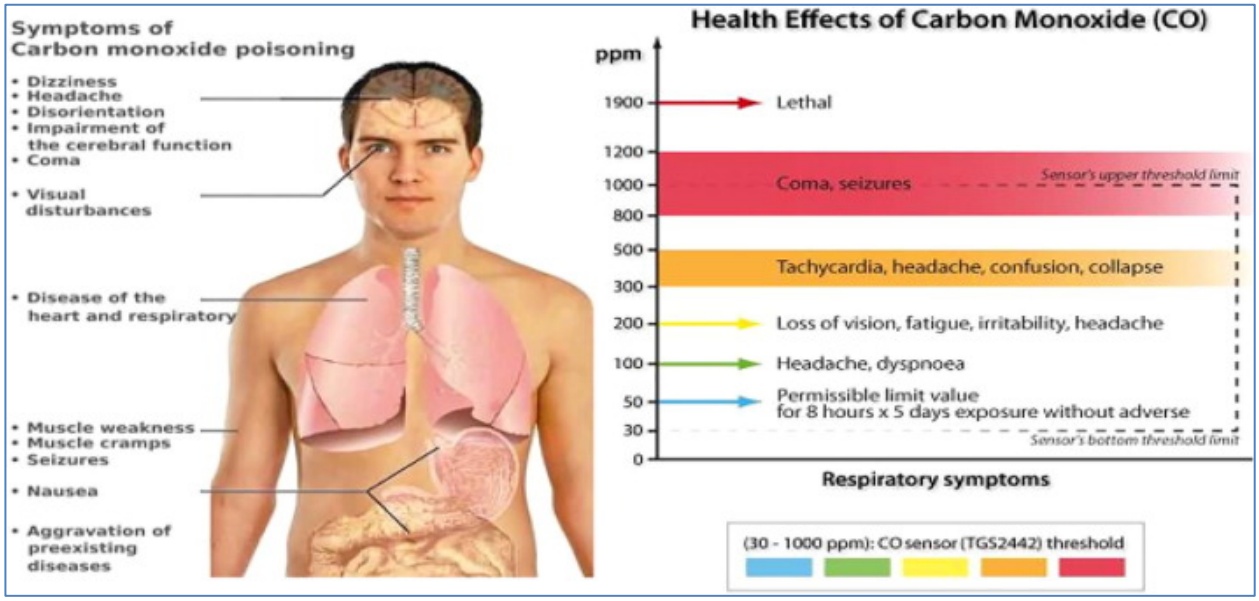

Figure A1. Effect of CO on human health.

Figure A2. Pictures of the system used for the catalytic tests.

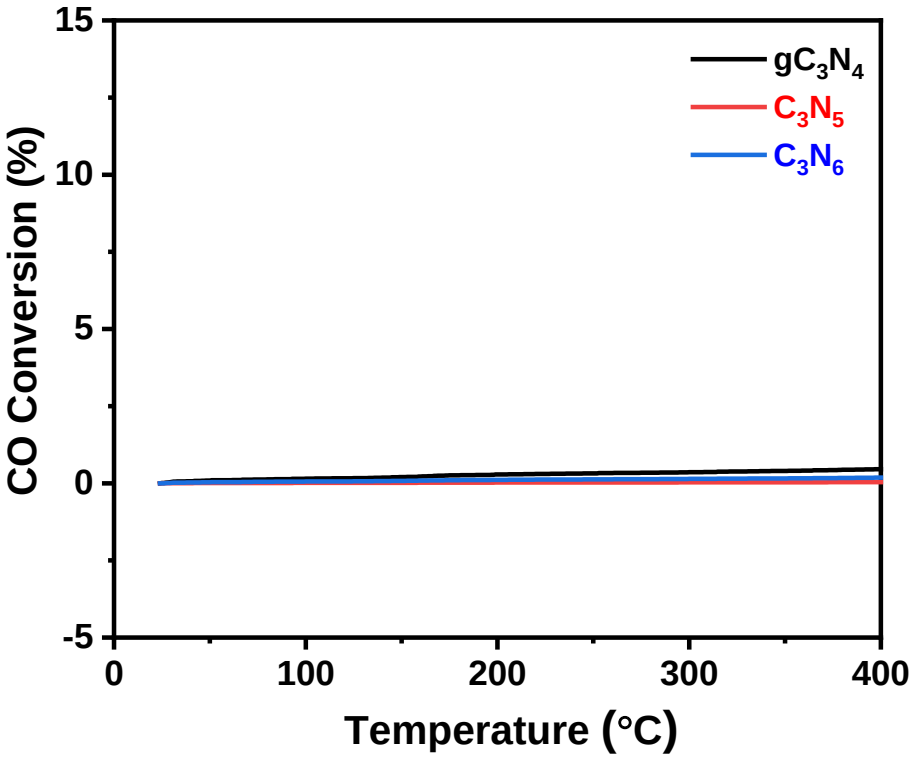

Figure A3. The catalytic activity of the C_3N_x phases